Second-harmonic generation of blue series excitons and magnetoexcitons in Cu_2O

A. Farenbruch,[1] D. Fröhlich,[1] H. Stolz,[2] D. R. Yakovlev,[1,3] and M. Bayer[1,3]
[1]*Experimentelle Physik 2, Technische Universität Dortmund, D-44221 Dortmund, Germany*
[2]*Institut für Physik, Universität Rostock, D-18059 Rostock, Germany*
[3]*Ioffe Institute, Russian Academy of Sciences, 194021 St. Petersburg, Russia*

(Received 5 May 2021; revised 13 August 2021; accepted 13 August 2021; published 30 August 2021)

Nonlinear optical studies of the yellow and green exciton series in Cu_2O have been reported for more than 40 years. Because of the band structure (the two highest even-parity valence and lowest conduction bands), the S excitons of the two lowest exciton series are dipole-forbidden for one-photon absorption and thus dipole-allowed for two-photon absorption. There is an odd-parity higher conduction band that leads with the two even-parity valence bands to the blue and violet exciton series. We report on second-harmonic generation (SHG) of the blue exciton series. The odd-parity S-exciton SHG is due to a dipole-quadrupole excitation and a dipole emission process. Because of their high oscillator strength density, polariton effects have to be taken into account, since resonances might be shifted to higher energies by up to 10 meV compared to the transverse exciton energies. The polariton dispersion for the blue excitons up to $n = 4$ is calculated and compared to the experimental results. In magnetic fields up to 10 T applied in a Voigt configuration ($\mathbf{B} \perp \mathbf{k}$), SHG of S excitons by a dipole-dipole excitation is observed, which is due to the admixture of dipole-dipole excited P excitons by the effective electric field from the magneto-Stark effect (MSE). From the analysis of the diamagnetic shift and the MSE interaction of the three-level system of $1S$, $2S$, and $2P$ excitons, we derive experimental results for the ratio $\langle r^2_{n,l}\rangle/\mu_X$ between the average of radius squared for the three states and the reduced exciton mass. For higher principal quantum number states, we observe magnetoexcitons up to $n = 8$. We analyze their magnetic field dependence and derive the electron effective-mass values for the crystalline orientations [111], [1$\bar{1}$0], and [001].

DOI: 10.1103/PhysRevB.104.075203

I. INTRODUCTION

Cuprous oxide (Cu_2O) is the material in which excitons were discovered almost 70 years ago [1], and it has remained a testbed for exciton spectroscopy, providing prominent exciton features with four exciton series of different symmetries recently studied by photoluminescence [2]. An unprecedented crystal quality allows the observation of Rydberg exciton states with a principal quantum number of up to $n = 30$ [3].

A schematic of the band structure with two valence and two conduction bands leading to the four known exciton series is shown in Fig. 1. The lowest exciton series (yellow series with a band gap of $E_g \approx 2.172$ eV) has recently gained a lot of interest [4,5]. The next higher exciton series (green series, $E_g \approx 2.30$ eV) arises from the next lower valence band (Γ_8^+ symmetry), split off by spin-orbit coupling from the highest valence band (Γ_7^+ symmetry) of the yellow series. Because of the even-parity lowest conduction band (Γ_6^+ symmetry), dipole transitions to S excitons are forbidden. Detailed symmetry considerations were first discussed in Ref. [6]. The lowest exciton ($1S$ exciton) can only be excited by an electric quadrupole transition [7]. Higher excitons from $n = 2$ (P excitons), however, can be excited by electric dipole transitions, but are expected to be much weaker than electric dipole S exciton transitions between bands of different parity [8]. In Ref. [1], a higher conduction band of Γ_3^- symmetry (Γ_8^- symmetry including spin) is reported, which was later confirmed by band structure calculations [9–11]; for recent work, see Ref. [12]. Excitons involving this Γ_8^- conduction band and the two uppermost valence bands (Γ_7^+ and Γ_8^+ symmetry) are commonly called the blue ($E_g \approx 2.62$ eV) and violet series ($E_g \approx 2.75$ eV) [13].

It turned out that the electric dipole allowed transitions to the blue exciton series were too strong to be measured in transmission on single crystals. The first measurements were done in reflection [14], yielding rather broad structures. Measurements in transmission require a sample thickness in the order of 0.1 μm [13]. Layers of Cu_2O were grown by oxidizing copper on quartz substrates, which are probably polycrystalline and strained [15,16]. There were no structures observable in absorption, which can be linked to series of blue excitons. In luminescence experiments with an excitation above the band edge in chemically etched bulk samples, two lines were observed that were assigned to the $1S$ and $2S$ excitons of the blue series [2]. The oscillator strength density of the blue electric dipole allowed exciton transitions ($\beta = 2.93 \times 10^{-3}$, Ref. [13]) is larger by a factor of 10^7 as compared to the yellow exciton transitions ($\beta = 3.1 \times 10^{-10}$, Ref. [17]). Their polariton character has to be taken into account leading to the well-known polariton dispersion relations $E(\mathbf{K})$ with resonance energies differing from the transverse (undisturbed by light field) exciton energies [18]. This was shown for the blue series in Ref. [19], where double resonant sum-frequency generation to the $1S$ exciton-polariton of the blue series was investigated. In these high-resolution experiments, the $1S$ exciton of the yellow series was resonantly excited by a quadrupole transition with use of a

single-frequency dye laser. With a tunable single-frequency infrared laser, an electric dipole transition from the 1*S* yellow exciton to the 1*S* blue polariton resonance was induced, which was detected by its emission of blue light.

Optical harmonics generation is a powerful tool to study electronic states in solids [20–22]. For this technique, commonly two-photon excitation is used, while it can be three or more photons as well, and one photon with double photon energy is detected. Second-harmonic generation (SHG) is a coherent process and differs strongly in this respect from the photoluminescence under two-photon excitation. For the SHG, the involved electronic state should have a finite matrix element for the two-photon excitation and single-photon emission, which make the process very sensitive to the symmetry of the electronic state and its modification under strain, and electric and magnetic fields. The SHG is also very informative for the exciton spectroscopy, as the nonlinear signals, which are typically weak, are resonantly enhanced at the exciton and exciton-polariton resonances [23]. Exciton states have been studied by SHG in various semiconductors such as GaAs, CdTe, (Cd,Mn)Te, EuTe, and ZnO, and model approaches for the symmetry analyses have been developed (see, e.g., Refs. [24,25]). An important role of exciton-polariton dispersion has been identified experimentally for second-, third-, and fourth-harmonic generation in ZnSe, GaAs, and CdTe [26,27]. We developed a technique for the SHG measurements using spectrally broad femtosecond laser pulses and a high-resolution spectrometer for the signal detection, which is extremely efficient and convenient for the exciton spectroscopy [28]. Being combined with the two-dimensional experimental approach for measuring the polarization dependence, SHG spectroscopy has been successfully applied for the detailed study of the yellow exciton series in Cu_2O [29], and it also allows us to identify the excited states of dark excitons [30,31]. Also the two-photon excitation of photoluminescence has been used to study excitons in Cu_2O [32–38]. The efficiency and polarization anisotropy of third-harmonic generation has been investigated in Ref. [39].

In this paper, we study in detail the exciton-polariton structure up to $n = 4$ of the blue series by means of optical second-harmonic generation. Only for excitation in low-symmetry directions (e.g., light wave vector $\mathbf{k} \parallel [111]$ and [112]) is the SHG signal observed, which can be assigned to the 1*S* polariton resonance. For these low-symmetry directions, we expect SHG of *S* excitons to be allowed by electric-quadrupole–electric-dipole two-photon excitation. Therefore, the polarization selection dependencies correspond to those of *P*-excitons of the yellow series, as it was shown in Ref. [29]. We observed a clear SHG resonance of the 1*S* blue exciton, and a dip in the region of an expected 2*S* polariton. There are no SHG structures detected at higher *n*.

In a magnetic field in Voigt configuration (magnetic field $\mathbf{B} \perp \mathbf{k}$), we observed clear resonances of the 1*S*, 2*S*, and 2*P* excitons and even detect weak SHG signals of magnetoexcitons up to $n = 6$. We explain these resonances by the magneto-Stark effect (MSE), which couples *nS* and *nP* excitons, and by the Zeeman effect (ZE), which couples states of the same parity [29].

For $\mathbf{k} \parallel [1\bar{1}0]$ and [001], the SHG by electric-quadrupole–electric-dipole excitation to the 1*S* blue exciton is forbidden [29], which is confirmed by our experiments. In a magnetic field in Voigt configuration, SHG from *S* and *P* excitons is enabled by the MSE, Γ_4^- ZE (coupling of Γ_4^- states), and Γ_5^+ ZE (coupling of Γ_5^+ states), which can be separated by a choice of the polarization configuration. The relevant polarization dependencies are derived in detail in Ref. [29]. For these orientations, we get blue exciton resonances up to $n = 8$.

The magnetic field dependence of the 1*S*, 2*S*, and 2*P* resonances is analyzed by a three-level model, where the diamagnetic shift of the resonances and the magneto-Stark (MS) coupling between the odd-parity 1*S*, 2*S* and the even-parity 2*P* exciton by the effective electric field is taken into account. From the analysis, we derive values for the ratio of the average exciton radius squared $\langle r_{1,0}^2 \rangle$, the effective exciton mass μ_X, and the exciton Bohr radius a_X, which are discussed with the results from the polariton and magnetoexciton analysis. In strong magnetic fields of up to 10 T, excited exciton states with weaker binding energy convert their diamagnetic shifts with a quadratic dependence on the magnetic field to an almost linear dependence of magnetoexcitons [40–42]. From the almost linear magnetic shift of the magnetoexcitons in high magnetic fields, we derive **K**-dependent effective electron mass values, with **K** being the combined electron-hole wave vector. From the electron masses for the different **K** directions, an effective exciton reduced mass is derived, which is compared to the results of band-structure calculations [11].

The paper is organized as follows: In Sec. II, we briefly describe the experiments. Section III is devoted to the polariton effect of blue exciton states in Cu_2O. In Sec. IV, several SHG mechanisms are introduced, and their spectral features are described. In Sec. IV A, we present the analysis of the experimental result of a three-level model for the magnetic field dependence of the 1*S*, 2*S*, and 2*P* resonances for $\mathbf{k} \parallel [1\bar{1}0]$. In Sec. IV B, we present the magnetoexciton analysis for $\mathbf{k} \parallel [001]$, $[1\bar{1}0]$, and [111] and we discuss the parameters derived with both methods. In Sec. V, we present conclusions and give an outlook on further experiments.

II. EXPERIMENT

The experimental setup for SHG measurements in magnetic fields is shown in Fig. 2. A detailed description of the setup is given in Refs. [28–30]. As compared to the setup described in Ref. [30], we use only the 0.5 m Acton spectrometer (80 μeV resolution) as a detection system. The pulses of a pump laser (200 fs, 30 kHz) are converted to 3.3 ps pulses via a second-harmonic bandwidth compressor and are tuned in wavelength by an optical parametric amplifier. The laser beam has a diameter of 3 mm and is focused by a 30 cm focal length lens onto the sample leading to a focus diameter of 120 μm calculated by Gaussian optics [43]. An average laser power of 100 mW corresponds in this case to a peak irradiance of about 10 GW cm^{-2} and an energy per pulse of 3 μj. The SHG light is collimated with a 25 cm focal length lens, and the parallel SHG beam is determined to be about the same diameter as the laser beam. The excitation laser has a spectral width of about 0.7 meV and generates a SHG spectrum in the sample with a spectral width of about 1.1 meV. Since the spectral width of the blue exciton resonances is on the order of 5–10 meV, we measure the SHG spectral dependences by

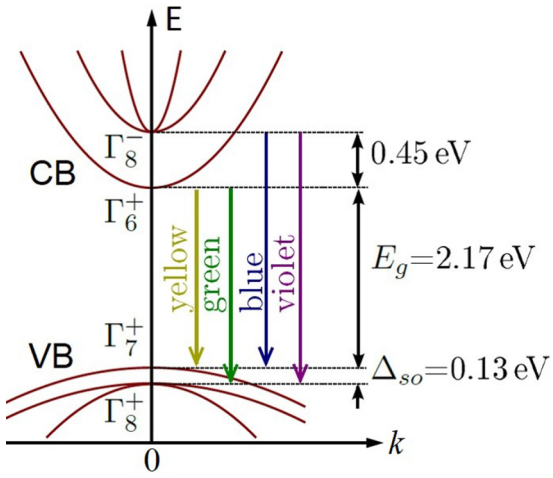

FIG. 1. Schematic band structure [5] of Cu_2O at the Γ point with conduction bands (CBs) and valence bands (VBs) and their symmetries leading to the yellow, green, blue, and violet exciton series.

tuning the laser from 1.265 to 1.34 eV (half of the exciton energy) and synchronously tuning the spectrometer by a LABVIEW program, so that the peak of the laser spectrum is always falling on the same pixel of the CCD detector. The output of this pixel is then taken as the SHG signal. An exemplary SHG spectrum for an excitation energy of 1.295 eV and a spectrometer set to 2.59 eV is shown as the gray area in Fig. 3(a). Depending on the mechanism involved, the SHG intensity of excitons exhibits a characteristic dependence on

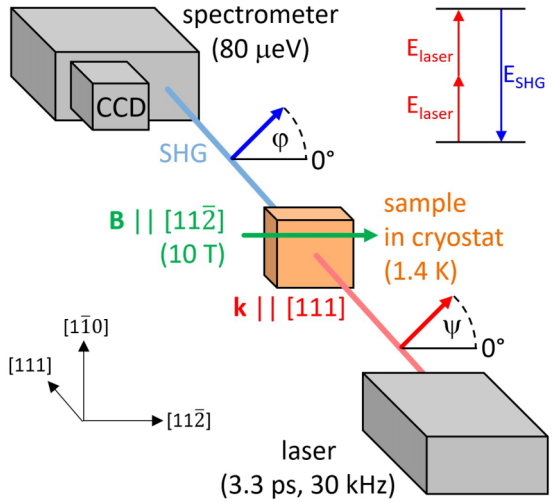

FIG. 2. Schematics of the experimental setup: The second harmonic is generated with 3.3 ps pulses at a repetition rate of 30 kHz. In a cryostat, the sample is cooled down to $T = 1.4$ K and exposed to a magnetic field up to 10 T applied in a Voigt configuration. A 0.5 m spectrometer with a CCD camera provides a spectral resolution of 80 μeV. The linear polarization angles of excitation laser light (ψ) and detected SHG light (φ) are set by Glan-Thompson polarizers and a $\lambda/2$ plate. The coordinate system in the bottom left corner shows the crystal orientation. The level diagram in the top right corner depicts the two-photon resonant excitation scheme of SHG illustrating the energies of the laser and SHG beam.

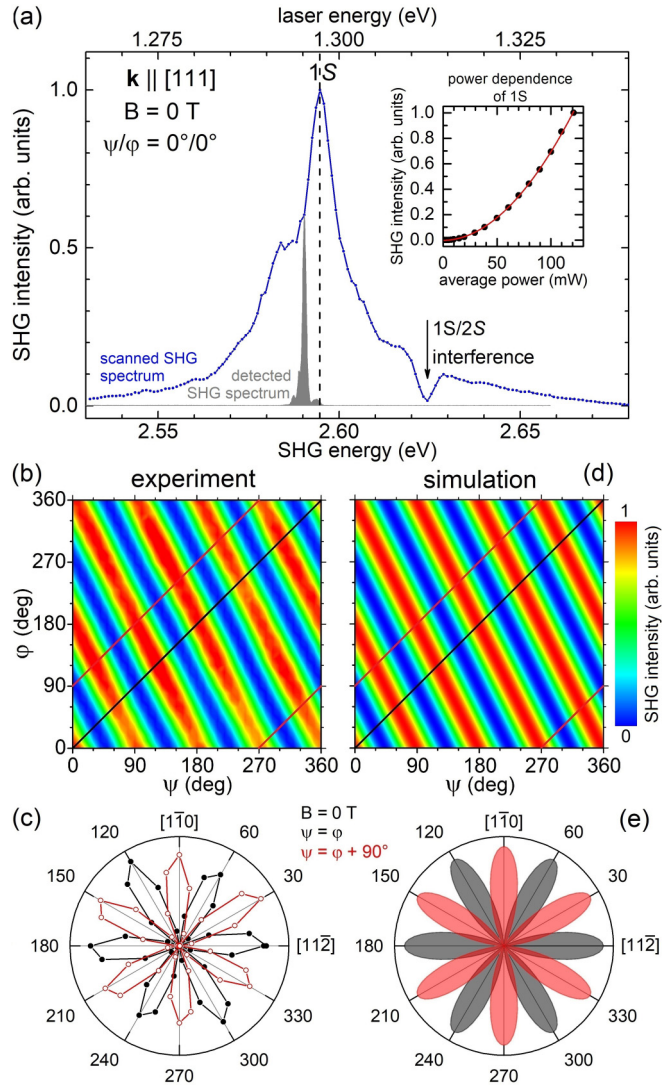

FIG. 3. (a) Scanned SHG spectrum of blue exciton-polariton states in Cu_2O measured for **k** ∥ [111]. The SHG spectrum for an excitation energy of 1.295 eV and a spectrometer setting of 2.590 eV, that is detected with the CCD camera, is shown as the gray area. The dip at 2.624 eV appears due to an interference of the 1*S* and 2*S* resonance. The inset shows the experimental SHG intensity (filled circles) depending on the average excitation power and a fit (red line) to the expected quadratic dependence. Experiment (b) and simulation (d) of the SHG intensity of the 1*S* exciton-polariton measured at 2.595 eV [dashed line in (a)] depending on the linear polarization angles of incoming (ψ) and outgoing (φ) light. Blue, light blue, green, yellow, and red indicate 0 %, 25 %, 50 %, 75 %, and 100 % of maximal SHG intensity, respectively. The polar plots (c) and (e) show the SHG intensity for parallel (black) and crossed (red) polarization configurations, as marked by the black and red tuning lines in the 2D plots.

the linear polarization angles of the incoming (ψ) and outgoing light (φ). A combination of a Glan-Thompson prism and a half-wave plate in the ingoing laser beam and the outgoing SHG beam allows us to rotate the linear polarization angles and measure full two-dimensional (2D) polarization diagrams, as was introduced in Ref. [29].

The samples are cut off from the same high-quality natural Cu_2O crystal from the Tsumeb mine in Namibia, and they have been used in previous studies of the yellow exciton series [5,7,17,27–31,40,44,45]. The samples are mounted strain-free [45] and have been immersed into superfluid helium with $T = 1.4$ K to provide optimal cooling. We study samples with different orientations to realize various experimental geometries for the incoming **k**-vectors of the laser beam and the magnetic field: $\mathbf{k} \parallel [111]$ and $\mathbf{B} \parallel [11\bar{2}]$, $\mathbf{k} \parallel [1\bar{1}0]$ and $\mathbf{B} \parallel [110]$, $\mathbf{k} \parallel [001]$ and $\mathbf{B} \parallel [110]$. The sample orientation is checked by x-ray diffraction measurements. All experiments are done in a Voigt configuration (magnetic field $\mathbf{B} \perp \mathbf{k}$), which leads to the magneto-Stark effect (MSE) in addition to the Zeeman effect (ZE), as is discussed in detail in Ref. [29]. The experimental geometries chosen allow us to separate crystallographic SHG and magnetic-field-induced SHG, as well as MSE- and ZE-induced SHG by making use of the 2D polarization dependence diagrams given in Appendix C of Ref. [29].

In Fig. 3(a) we show the SHG spectrum of the blue excitons measured for $\mathbf{k} \parallel [111]$ and $B = 0$ T. The gray area shows the SHG signal at a fixed laser energy of 1.295 eV indicating the spectral shape of the picosecond laser. The spectrum is measured by scanning the laser excitation in steps of 0.55 me V SHG energy across the spectral region of 2.53–2.68 eV. For each laser energy, the maximal intensity of the SHG signal is plotted. The synchronous tuning of the laser and the spectrometer setting is achieved by a LABVIEW program.

The SHG spectrum of the blue 1*S* exciton has a maximum at 2.595 eV. As can be seen in Fig. 3(a), there is a shoulder at 2.585 eV in the SHG spectrum in case of the crystallographic SHG at $B = 0$ T. Since its peak agrees roughly with that of the transverse exciton, it may originate from the direct emission of the blue exciton. While inside the crystal the excitation of these states is forbidden by wave-vector conservation [8], in the surface layer some disorder may occur due to the treatment in preparation. This suspends strict **k** conservation and leads to direct excitation of transverse excitons. Since its relative intensity to the 1*S* signal depends on sample position, it is not considered further.

We assign the structure at 2.624 eV to a resonance effect between the 1*S* state and the 2*S* state, as will be discussed in Sec. III.

In Figs. 3(b) and 3(c), the polarization dependence of the crystallographic SHG intensity is shown. The experimental results are measured at the energy of the 1*S* exciton-polariton, as marked by the dashed line in Fig. 3(a), in steps of $\psi, \varphi = 10°$. The 2D diagram shows the SHG polarization dependence of all possible ψ/φ configurations with an applied interpolation to the measured data points. Blue indicates zero and red indicates maximum SHG intensity. The SHG intensity along the black tuning line corresponds to parallel linear polarizations of incoming laser and outgoing SHG light, which are rotated simultaneously from 0° to 360° (parallel configuration). It is plotted as a function of ψ in the polar diagram below and shows a sixfold symmetry with a maximum at 0°. The configuration of orthogonal linear polarizations of an incoming laser and outgoing SHG light (crossed configuration) is represented by the red tuning line in the 2D diagram. Its SHG intensity is plotted as a function of ψ in the polar diagram below and shows a sixfold symmetry with a maximum at 90°. The simulation of crystallographic SHG is calculated according to Eq. (14) from Ref. [29] for the quadrupole-dipole SHG and visualized by the 2D and polar diagram in Figs. 3(d) and 3(e). The simulation is in good agreement with the experimental results.

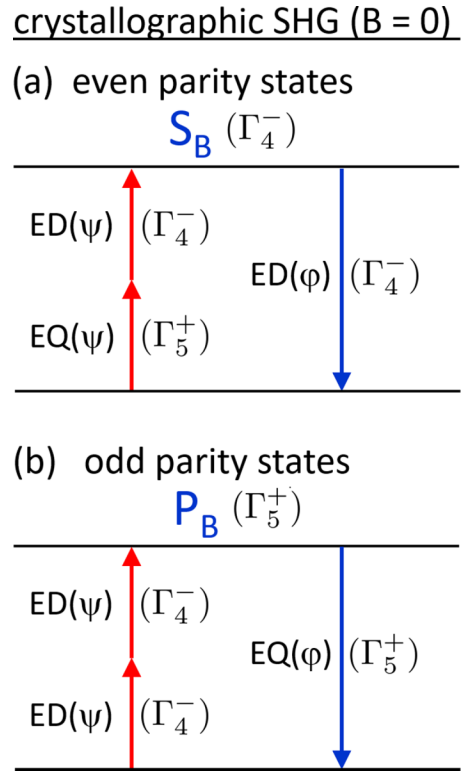

FIG. 4. Schemes of crystallographic SHG mechanisms of blue *S* (a) and *P* excitons (b) at zero magnetic field involving electric dipole (ED) and electric quadrupole (EQ) transitions. See Ref. [29] for more details.

The crystallographic SHG mechanism for blue *S* and *P* excitons is sketched in Fig. 4 in energy-level diagrams. An analogy can be drawn between the blue and yellow excitons. For the yellow excitons, the mechanisms were already discussed in great detail in Ref. [29]. The blue *S* excitons can be treated as the yellow *P* excitons, as their main optically active components have the same Γ_4^- symmetry. The same is valid for the blue *P* and yellow *S* excitons with Γ_5^+ symmetry.

The two up-arrows represent the two-photon excitation process. They start from the initial state of an unexcited crystal and point to the exciton state [S_B or P_Y with Γ_4^- symmetry in Fig. 4(a) and P_B or S_Y with Γ_5^+ symmetry in Fig. 4(b)]. The down-arrow represents the one-photon emission process. The arrows are labeled by the type of light-matter interaction [electric dipole (ED) and electric quadrupole (EQ)], its symmetry (Γ_4^-, Γ_5^+), and the linear polarization angles (ψ, φ) of the photons involved.

III. POLARITON EFFECT OF BLUE EXCITONS

In the following, we will derive expressions for the oscillator strength density, the radiative lifetime, and the polariton dispersion of the blue excitons up to $n = 4$. Because of their large oscillator strength density, blue and violet excitons have to be considered as polaritons, which is important for understanding their key properties.

As the S states of different quantum numbers n are lying very close together (exciton Rydberg energy 57.1 me V; see Appendix A), one has to take into account their total contribution to the dielectric function. The next higher state (the violet excitons) with large oscillator strength density is quite far away (energy distance of 130 meV), so its contribution can be taken into account in the background dielectric function ε_b.

Starting from the classical exciton-polariton theory [18], we have

$$\frac{c_0^2 K^2}{\omega^2} = \varepsilon(\mathbf{K}, \omega) = \varepsilon_b + \sum_{n=1}^{N} \frac{4\pi \beta_n E_{Xn}^2(\mathbf{K})}{E_{Xn}^2(\mathbf{K}) - (\hbar\omega)^2 - i\hbar\omega\Gamma_n}. \tag{1}$$

The energy dispersion of the excitons is given by

$$E_{Xn}(\mathbf{K}) = E_{0,n} + \frac{\hbar^2}{2M_n}\mathbf{K}^2, \tag{2}$$

where $E_{0,n}$ is the exciton energy at $K = 0$, M_n is the total exciton mass, c_0 is the vacuum speed of light, $\hbar$ is the reduced Planck constant, $\mathbf{K}$ is the polariton wave vector, ω is the frequency, and Γ_n is a homogeneous broadening. The number N of exciton states, over which the summation is carried out, is in principle infinite. Here we only take into account the $n = 1, 2, 3, 4$ blue S excitons. The parameters β_n characterize the strength of the exciton-photon interaction and are related to the oscillator strength density f_n/V (the volume is conventionally set to the volume of the elementary cell $V = a_l^3$ with the lattice constant a_l) by

$$\beta_n = \frac{\hbar^2 e^2}{4\pi\varepsilon_0 m_0 E_{Xn}^2}\frac{f_n}{V}. \tag{3}$$

ε_0 is the vacuum permittivity, and e and m_0 refer to the electron charge and mass, respectively.

Due to the proportionality of oscillator strength density to the absolute square of the exciton wave function at electron-hole distance = 0 [18], only S states are dipole-allowed for the blue and violet excitons. The splitting between longitudinal and transverse excitons (LT splitting) is directly related to the oscillator strength density and is given by

$$\Delta E_{\mathrm{LT},n} = \frac{\hbar^2 e^2}{2\varepsilon_0\varepsilon_b m_0 E_{Xn}}\frac{f_n}{V}, \tag{4}$$

with the background dielectric constant ε_b. For the calculation of the polariton dispersion relations as solutions of Eq. (1), we have to know the β_n parameters, the energies of the states, their damping, and the background dielectric constant.

The exciton energies at $K = 0$ (transverse energies) for the blue $1S$ and $2S$ states and for the violet $1S$ state were obtained recently from photoluminescence measurements [2] as $E_{0,1S,B} = 2.5829$ eV, $E_{0,2S,B} = 2.6209$ eV, and $E_{0,1S,V} = 2.7191$ eV, the indices B (V) denoting blue (violet) states. Due to the high accuracy of our experiments and our polariton calculations, we could determine the values for the $1S$ and $2S$ blue states to 2.579 26 and 2.619 21 eV, respectively, as listed in Table IV.

The oscillator strength per unit cell for the blue $n = 1$ state was given in Ref. [13] as 13.7×10^{-3} at $T = 4.3$ K, from which follows $\beta_{1SB} = 2.93 \times 10^{-3}$. A detailed investigation of the complex dielectric constant by ellipsometry [46] gave $\beta_{1SB} = 4.93 \times 10^{-3}$, however at room temperature. To achieve quantitative agreement with our experiments, we have to take as values of the oscillator strength per unit cell for the blue $1S$ exciton $f_{\mathrm{osc,B}}/a_l^3 = 0.017\,638$, corresponding to $\beta_{1SB} = 3.77 \times 10^{-3}$, which is close to the averages of the literature data. In the hydrogen model, the dependence on quantum number is given by

$$\beta_{n,S} = \beta_{1S}/n^3. \tag{5}$$

From this we obtain for the LT splitting $\Delta E_{\mathrm{LT},B}(n) = 3.83\ \mathrm{meV}/n^3$ for the blue exciton.

The damping of the states, which is relevant to polariton damping [18], can be obtained simply from the linewidth of the SHG process [47,48]. We obtain $\Gamma_{1SB} = 13.3$ meV and $\Gamma_{2SB} = 7.6$ meV from a fit of two Lorentzians to the Γ_5^+ ZE spectrum (red line) shown later in Sec. IV in Fig. 8(c). We will use the following empirical law, which reproduces the experimentally found linewidths for the $1S$ and $2S$ polaritons and allows us to extrapolate the damping for higher n:

$$\Gamma(n) = \frac{13.9}{n}\ (\mathrm{meV}). \tag{6}$$

Obviously, the ratio for the different quantum states does not follow the law for the lifetime $\hbar/\Gamma(n)$ derived in Ref. [49] indicating that the dominant scattering process is different from the case for the yellow P states. The origin of this effect is at present unclear and would require further investigations, which are outside the scope of this paper.

To obtain a consistent set of transverse exciton energies, we use a simplified model that allows us to take the central cell corrections due to the frequency dependence of the dielectric function in the range of the exciton binding energies into account (for details, see Appendix A). This allows us to determine the Rydberg energy of the blue excitons as $E_{\mathrm{Ryd}} = 57.1$ meV. One can simplify the dispersion relation (1) by applying the rotating wave approximation, i.e., assuming $\hbar\omega \approx E_X$. Then we can write

$$E_X^2 - (\hbar\omega)^2 = 2E_X(E_X - \hbar\omega) \tag{7}$$

and get the dispersion relation

$$\varepsilon(\mathbf{K}, \omega) = \varepsilon_b + \sum_{n=1}^{N} \frac{2\pi \beta_n E_{Xn}(\mathbf{K})}{E_{Xn}(\mathbf{K}) - \hbar\omega - i\frac{\Gamma_n}{2}}. \tag{8}$$

For the problem of the background dielectric constant due to the large oscillator strength densities of blue and violet excitons, we follow the thorough analysis of different contributions in Ref. [46]. From this we can estimate the background dielectric constant. The dominant contribution is from the exciton states at the X and M point of the Brillouin zone at $E_{1X} = 3.45$ eV and $E_{1M} = 4.25$ eV. Furthermore, the contribution of the transitions into the blue continuum and

violet exciton and continuum states is important. To facilitate the implementation in the program for the calculation of the polariton states, we fitted a Sellmeier equation to the background dielectric constant (for details, see Appendix B). This is given by

$$\varepsilon_b(E) = 4.202 + \frac{2.564}{1 - \left(\frac{E[\mathrm{eV}]}{3.166}\right)^2}. \tag{9}$$

For the calculation of the polariton dispersions, we used the method of Cho [50]. Here we have to distinguish between two cases [51]: (i) The quasiparticle case, where polaritons with a well-defined wave vector are created, and (ii) the forced harmonic case, where polaritons are created by an external harmonic driving source, e.g., a laser wave. The latter is appropriate for transmission experiments, while the first applies, e.g., to two-photon absorption. The existence of polaritons in the quasiparticle situation is governed by the condition that the Rabi energy [40]

$$\hbar\Omega_R = \sqrt{\frac{\Delta E_{\mathrm{LT}} E_X(0)}{2}} \tag{10}$$

is larger than the damping Γ (temporal coherence). In the forced harmonic situation, polaritons exist (in the sense that one can observe an anticrossing of the dispersion relations) if the following condition is fulfilled (spatial coherence) [18]:

$$\Gamma < \sqrt{\frac{8\Delta E_{\mathrm{LT}}\varepsilon_b}{M_X c^2}} E_X^2(0). \tag{11}$$

Inserting the quantities for the blue and violet excitons, the condition for the forced harmonic situation is not fulfilled, so that the polariton model is not necessary to describe one-photon transmission experiments.

In contrast, the condition for the quasiparticle situation is satisfied (Rabi energy of 70 meV compared to 13 meV damping) so that a polariton description is necessary in multi-photon experiments. In the SHG considered here, two infrared photons with energy half of that of the excitons and with well-defined wave vectors are combined by a $\chi^{(2)}$ susceptibility to a quasiparticle excitation also with a well-defined wave vector. One has to solve Eq. (1) not for a fixed photon energy E, rather one has to look for solutions with a fixed wave number K. The quasiparticle solutions obtained in this way are shown in Fig. 5. The parameters for the calculation are listed in Table I. Despite the large damping in time, we clearly see the dispersion of polaritons [Fig. 5(b)].

The laser tuning line $E(\mathbf{K})$, which describes the dispersion of two infrared photons, is determined by the refractive index $n_b(E/2) = \sqrt{\varepsilon_b}$ at the laser energy $E/2$. The wave number K of the polaritons is thus given by $K(E) = 2n_b(E/2)/\hbar c \cdot E/2$, and for the $E(k)$ tuning line we obtain

$$E(k) = \frac{c}{n_b(\frac{E}{2})}\hbar k, \tag{12}$$

which is plotted as the gray line in Fig. 5(a).

We see a drastic shift of these resonances from both the transverse exciton energy and also from the longitudinal excitons, which coincide with the transverse polaritons at $K = 0$. This shift is especially interesting for the $2S$ resonance, as it coincides with the second upper polariton branch. Therefore,

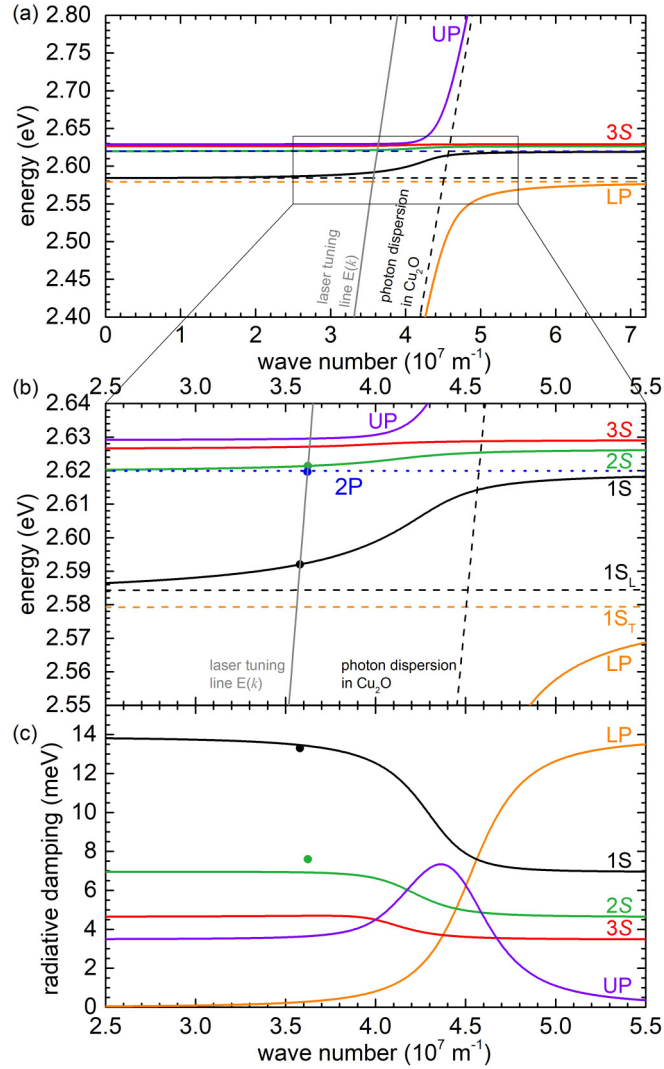

FIG. 5. Quasiparticle solutions for the $1S$ to $4S$ blue exciton polaritons: Orange lines show the lower- and the black lines the upper-polariton branch of the $1S$ resonance. The green, red, and violet lines represent the $2S$, $3S$, and $4S$ exciton-polaritons, respectively. (a) Real part of the polariton self-energy as a function of wave number, which is zoomed in panel (b). The gray line refers to the laser tuning line $E(k)$ as given by Eq. (12), and the blue dashed line refers to the $2P$ dispersion. Due to its zero oscillator strength density, the $2P$ exciton is not affected by the polariton effect, so that its energy is given by the resonance energy itself. Filled circles mark the zero-field resonances as measured in SHG ($1S$, $2S$, and $2P$ in Fig. 9). (c) Radiative polariton damping (temporal decay) as a function of wave number obtained from polariton theory [Eq. (1)]. The black line refers to the first upper polariton branch with a transition from the high damping of the $1S$ exciton state at $K = 0$ to that of the $2S$ exciton at large K. The dots represent the polaritons excited by the SHG process, indicating the almost complete exciton character of the polariton here.

the dip in the SHG intensity at 2.624 eV in Fig. 3(a) cannot be explained as a simple reabsorption of the light produced by SHG of the $1S$ exciton-polariton, but as a resonance of the $1S$ and $2S$ exciton-polaritons that have here the same wave vector so that interference, which then obviously must be

TABLE I. Parameters used for quasiparticle solutions according to Eq. (1) as shown in Fig. 5. The dielectric constants are calculated according to Eq. (A2). The exciton binding energies E_{Bn} are calculated according to Eq. (A1) with a band gap of $E_g = 2.6326$ eV and a reduced exciton mass of $\mu_X = 0.228 m_0$. The exciton damping parameters Γ_n are calculated according to Eq. (6). The exciton-photon interaction parameters β_n are calculated according to Eq. (5), while the longitudinal-transverse splitting is calculated according to Eq. (4).

n	$\tilde{\varepsilon}(E_{Bn})$	E_{Bn} (meV)	Γ_n (meV)	β_n	$\Delta E_{\mathrm{LT},n}$ (meV)
1	7.63	53.30	13.9	3.768×10^{-3}	3.93
2	7.62	13.35	7.64	4.582×10^{-4}	0.491
3	7.41	6.29	4.16	1.351×10^{-4}	0.146
4	7.38	3.56	2.70	5.689×10^{-5}	0.061

destructive, is possible. This interpretation is substantiated by the observation that the minimum is not at the exact position of the 2*S* resonance (2.6214 eV as shown in Fig. 9) but shifted to higher energies by almost 3 meV.

IV. BLUE EXCITONS IN A MAGNETIC FIELD

We now turn to the magnetic-field-induced SHG of blue series excitons. External fields lower the symmetry of the system and can therefore induce an additional contribution to the SHG signal. The magnetic field **B** of Γ_4^+ symmetry couples states of the same parity, e.g., *P* excitons of Γ_5^+ symmetry or *S* excitons of Γ_4^- symmetry, which we refer to as the Γ_5^+ and Γ_4^- Zeeman effect, respectively. Due to the motion of the excitons perpendicular to the magnetic field, the Lorentz force acts on the electron and hole in opposite directions and causes a separation of the charge distributions, which leads to the effective electric field $\mathbf{E}_{\mathrm{MSE}} \sim \mathbf{k} \times \mathbf{B}$ of the magneto-Stark effect. Due to its Γ_4^- symmetry, the effective electric field couples states of opposite parity. These three mechanisms (Γ_4^- ZE, Γ_5^+ ZE, and MSE) are sketched in Fig. 6 in energy level diagrams equivalent to the crystallographic mechanisms, as shown in Fig. 4. Horizontal arrows represent the coupling between the states by the external field.

To study the mechanisms of magnetic-field-induced SHG without the interference with crystallographic SHG, we present two options to suppress the latter: (i) In a low-symmetry crystal axis, e.g., [111] or [11$\bar{2}$], a certain choice of a polarization configuration can suppress the crystallographic and allow magnetic-field-induced SHG signals, and (ii) choice of **k** along a crystal axis, in which crystallographic SHG is forbidden for any polarization configuration due to high symmetry, e.g., [001] and [1$\bar{1}$0]. In the experimental geometry, **k** ∥ [111] and **B** ∥ [11$\bar{2}$], option (i) applies. In this orientation, crystallographic SHG is present, e.g., at 0°/0° as shown in Fig. 3(a), but it can be suppressed at, e.g., 90°/90°. The magnetic-field-induced SHG mechanisms cannot be separated from each other by a choice of the polarization configuration, and they are all interfering with their maximum contribution at, e.g., 90°/90°. The simulations of 2D polarization diagrams of each SHG mechanism are shown in Fig. 13 in Appendix C.

Figure 7(a) shows the series of magnetic-field-induced SHG spectra for magnetic fields varied from 0 up to 10 T in steps of 1 T. In the $B = 0$ spectrum, no resonances are expected. The reason for the weak 1*S* signal might be a small misalignment of the sample or the polarizers. In finite magnetic fields, the 2*P* exciton shows a stronger SHG signal as compared to the 1*S* exciton, as the 2*S*-2*P* MS-coupling is stronger than the 1*S*-2*P* MS-coupling due to the smaller energy difference between the corresponding exciton states. The magnetic field dependence of the induced 1*S* and 2*P* exciton SHG [see Fig. 7(a)] and of the 2*S* exciton dip [see Fig. 3(a)] is analyzed in Sec. IV A. On the high-energy side of the 2*S* exciton-polariton, several oscillations are emerging with increasing magnetic field. Based on the situation in the [1$\bar{1}$0] direction, in which only ZE-induced magnetoexciton signals are seen, we assign these resonances to *S*-type magnetoexcitons. Their magnetic field dependence is analyzed in Sec. IV B.

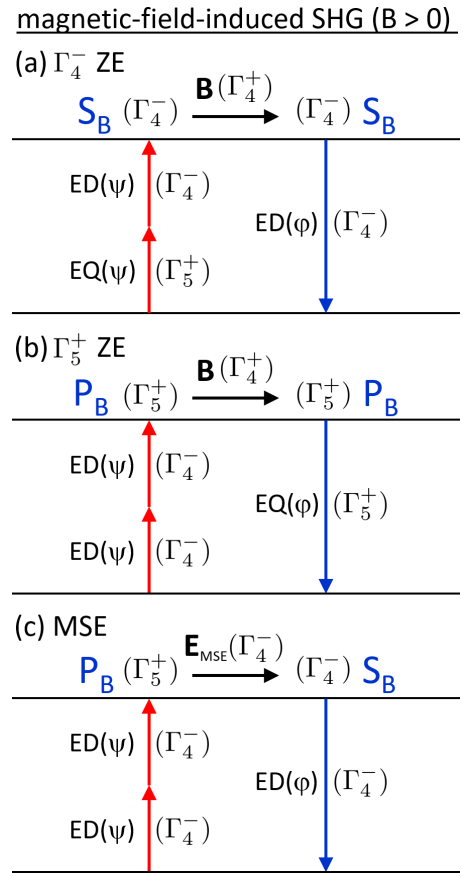

FIG. 6. Schemes of SHG mechanisms of blue excitons in a magnetic field: Magnetic-field-induced SHG by ZE of Γ_4^- (a) and Γ_5^+ (b) states and by MSE (c). See Ref. [29] for more details.

For a measurement of the polarization dependence of the magnetic-field-induced contribution without an interference with the crystallographic SHG, one has to set the two-photon excitation energy to the $1S - 2S$ interference dip at 2.624 eV, as seen in Fig. 3(a) and marked by the dashed line in Fig. 7(a), because it is the only energy at which the crystallographic SHG is suppressed for all polarization configurations. The polarization dependence at $B = 10$ T of the SHG intensity of the 2*P*-2*S* mixed exciton resonance is shown in Figs. 7(c) and 7(d). The simulation in Figs. 7(e) and 7(f) takes an

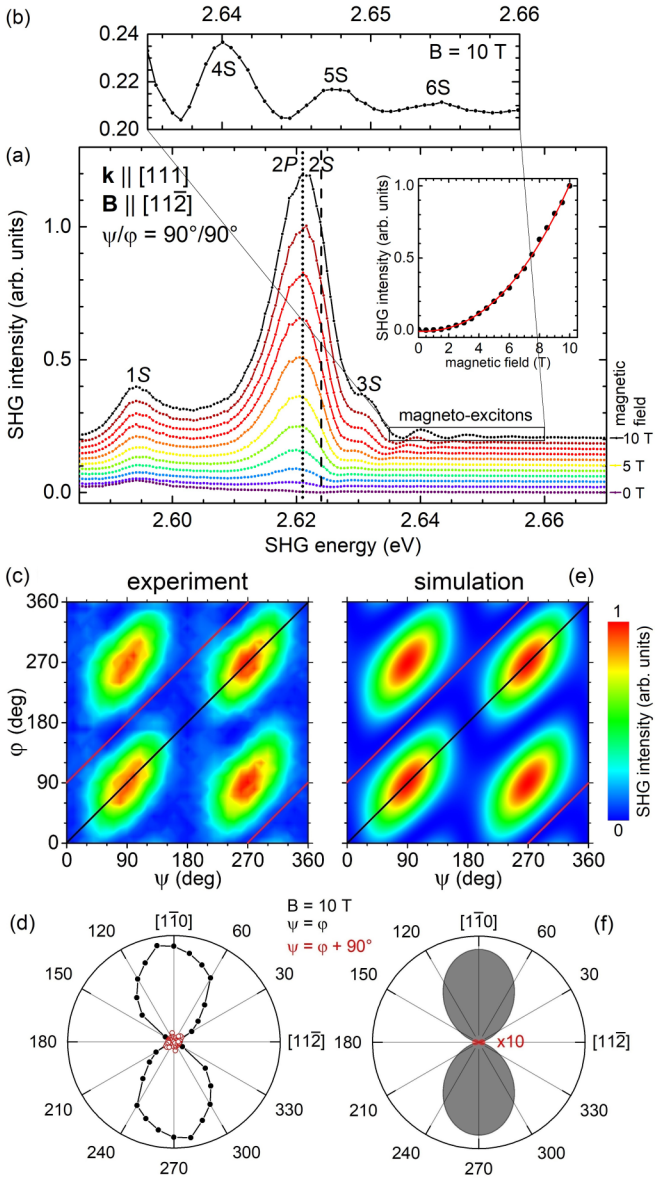

FIG. 7. SHG spectra of blue excitons in magnetic fields up to 10 T for the experimental geometry: **k** ∥ [111] and **B** ∥ [11$\bar{2}$]. (a) Exciton and magnetoexciton resonances. The inset shows the quadratic dependence of 2*P* (dotted line at 2.621 eV) SHG intensity on magnetic field. (b) Zoomed spectra of magnetoexcitons for $n = 4, 5, 6$ at $B = 10$ T. Experiment (c) and simulation (e) of 2D plots of SHG polarization dependence of 2*S* shoulder [dashed line in panel (a) at 2.624 eV] at $B = 10$ T. The polar plots (d) and (f) show the SHG intensity for parallel (black) and crossed (red) polarization configurations, as marked by the black and red tuning lines in the 2D plots.

interference of the normalized contribution of the MSE and ZE,

$$I^{\mathrm{SHG},[111]}_{\mathrm{interf.}}(\psi,\varphi) = \left|\alpha_1 \frac{O_{\mathrm{ZE}}(\psi,\varphi)}{|\widehat{O}_{\mathrm{ZE}}|} + \beta_1 \frac{O_{\mathrm{MSE}}(\psi,\varphi)}{|\widehat{O}_{\mathrm{MSE}}|}\right|^2, \quad (13)$$

at a ratio of $\alpha_1/\beta_1 = 4/3$ into account and is in good agreement with the experiment. For the simulation one has to add up the amplitudes of the two possible SHG mechanisms before taking the absolute value squared. O_i are the operators, which describe the corresponding SHG mechanism, and $\widehat{O}_i$ are their amplitudes. The coefficients α_1 and β_1 represent their relative contribution. For this interference simulation, the Γ_4^- ZE and Γ_5^+ ZE are not treated separately, as their polarization dependence is identical in this crystal orientation, as can be seen in Figs. 13(c) and 13(d) of Appendix C.

We now turn to the experimental configuration **k** ∥ [1$\bar{1}$0] and **B** ∥ [110], for which option (ii) applies. A characteristic of this geometry is that specific polarization configurations allow a complete separation of the three magnetic field SHG mechanisms as shown in Figs. 14(c), 14(d), and 14(e). Figure 8 shows the spectral features of the SHG induced by these three mechanisms.

For this experimental geometry, the crystallographic SHG is absent for all polarization configurations, as confirmed by the black line in Fig. 8(a) measured at zero magnetic field. At a magnetic field of 10 T and $\psi/\varphi = 90°/90°$, a strong SHG signal (blue line) appears, which is induced by the Γ_4^- ZE mechanism sketched in Fig. 6(a). The peak at 2.621 eV is assigned to the 2*S*/2*P* mixed exciton-polariton with a full width at half-maximum (FWHM) of 10.5 me V acquired by a fit of two Lorentzians to the SHG spectrum. The less intense peak at 2.592 eV is assigned to the 1*S* exciton-polariton. Compared to the spectrum shown in Fig. 3(a), the low-energy shoulder, which was assigned to the luminescence from the transverse exciton, is absent. Energetically above the 2*S*/2*P* peak, several resonances up to $n = 8$ appear, which we assign to magnetoexcitons in the high-field regime [see the zoom in Fig. 8(b)]. The magnetic field dependence of these magnetoexcitons is shown in Fig. 10 and analyzed in Sec. IV B.

Figure 8(c) shows SHG spectra induced purely by the weaker Γ_5^+ ZE (red line) and MSE (green line) as sketched in Figs. 6(b) and 6(c), respectively. The 2*S* exciton-polariton SHG signal of the Γ_5^+ ZE (polarization configuration of 0°/90°) is 17 times weaker than that of the Γ_4^- ZE shown in Fig. 8(a), and the 1*S* resonance is twice as intense as the 2*S* resonance. The line (FWHM of 7.6 me V) of the 2*S* exciton-polariton is narrower in comparison to the dominant Γ_4^- ZE. This is due to the lack of a 2*P* exciton contribution to the SHG signal in this polarization configuration. The magnetoexcitons are not as clearly visible here, mostly due to lower signal intensity.

The 2*P* exciton SHG signal of the MSE in Fig. 8(c) (polarization configuration of 45°/0°) is 10 times weaker than that of the Γ_4^- ZE [blue line in Fig. 8(a)], and the ratio of 1*S* and 2*S* SHG signals is comparable to that of the dominant Γ_4^- ZE. The line (FWHM of 9.7 me V) of the $n = 2$ resonance of the MSE (green line) is also narrower than that of the Γ_4^- ZE (blue line) and about 2 meV lower in energy compared to the 2*S* exciton of the Γ_5^+ ZE (red line). It is therefore assigned to the 2*P* exciton, because it is not affected by the polariton effect and is therefore energetically lower than the 2*S* exciton polariton [Fig. 5(b)]. The splitting is explained by the repulsion of the 2*S* and 2*P* states, caused by the MS coupling. A signal of the magnetoexcitons is absent in the MSE spectrum (green line).

Figures 8(d), 8(e), and 8(f) show the SHG spectra of the 1*S*, 2*P*, and 2*S* resonances induced at magnetic fields of 2–10 T by the Γ_4^- ZE, Γ_5^+ ZE, and MSE, respectively. The SHG signals

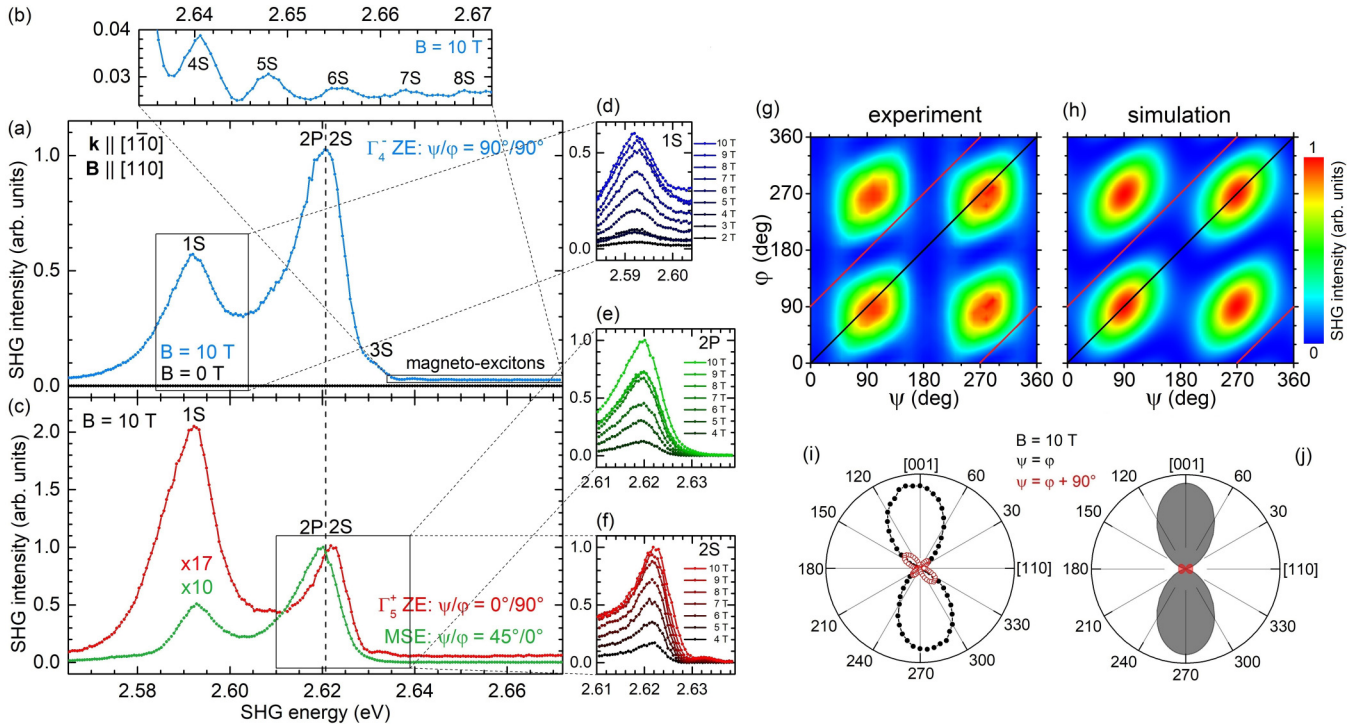

FIG. 8. (a) SHG spectrum at zero magnetic field (black line) shows no signal for the experimental geometry: **k** ∥ [1$\bar{1}$0] and **B** ∥ [110]. At $B = 10$ T, SHG (blue line) is induced by the Γ_4^- ZE at a polarization configuration of 90°/90°, showing a $2S/2P$ mixed exciton resonance, a $1S$ exciton-polariton signal, and magnetoexcitons up to $n = 8$, which are zoomed in panel (b). Panel (c) shows the SHG spectra of the Γ_5^+ ZE (0°/90°) and the MSE (45°/0°), which are at 2.621 eV smaller by a factor of 17 and 10 compared to the dominant Γ_4^- ZE signals shown in panel (a). Magnetoexcitons are absent in the MSE spectrum. Panels (d), (e), and (f) show the SHG spectra of $1S$, $2P$, and $2S$ resonances for magnetic fields of 2–10 T. Panels (g) and (h) show the 2D plots of experimental and simulated SHG polarization dependence of the $2S/2P$ resonance at 2.621 eV and $B = 10$ T. The polar plots in panels (i) and (j) show the SHG intensity for parallel (black) and crossed (red) polarization configurations, as marked by the black and red tuning lines in the 2D plots.

get weaker for decreasing magnetic fields. The magnetic field shift of the resonance energies is analyzed in Sec. IV A and shown in Fig. 9.

The polarization dependence at $B = 10$ T of the SHG intensity of the $2S$-$2P$ mixed exciton resonance at 2.621 eV [dashed line in Fig. 8(a)] is shown in Fig. 8(g). As can be seen in Figs. 8(a) and 8(c), all three mechanisms induce SHG at this energy and are therefore interfering. The simulations of 2D polarization diagrams of each individual SHG mechanism are shown in Figs. 14(c), 14(d), and 14(e) of Appendix C. The experimental 2D diagram in Fig. 8(g) shows the greatest similarity with the simulation of the Γ_4^- ZE in Fig. 14(c) with slight distortions, which can be explained by smaller contributions of the Γ_5^+ ZE and MSE. Therefore, the simulation of the polarization-dependent SHG intensity

$$I_{\text{interf.}}^{\text{SHG},[1\bar{1}0]}(\psi,\varphi) = \left|\alpha_2 \frac{O_{\Gamma_4^-\text{ZE}}(\psi,\varphi)}{|\widehat{O}_{\Gamma_4^-\text{ZE}}|} + \beta_2 \frac{O_{\text{MSE}}(\psi,\varphi)}{|\widehat{O}_{\text{MSE}}|} + \gamma_2 \frac{O_{\Gamma_5^+\text{ZE}}(\psi,\varphi)}{|\widehat{O}_{\Gamma_5^+\text{ZE}}|}\right|^2 \tag{14}$$

takes into account an interference of the normalized contributions of the Γ_4^- ZE, MSE, and Γ_5^+ ZE. Figure 8(h) shows the simulated polarization diagram with the ratios $\alpha_2/\beta_2 = 3.5$ and $\alpha_2/\gamma_2 = 4$, which are in good agreement with the experimental intensity ratios of $I^{\text{SHG}}_{\Gamma_4^-\text{ZE}}/I^{\text{SHG}}_{\text{MSE}} = 10 \approx 3.5^2$ and $I^{\text{SHG}}_{\Gamma_4^-\text{ZE}}/I^{\text{SHG}}_{\Gamma_5^+\text{ZE}} = 17 \approx 4^2$, respectively, as shown in Figs. 8(a) and 8(c).

The polar diagrams in Figs. 8(i) and 8(j) show the parallel and crossed polarization configurations as marked by the black and red tuning lines in the 2D plots, respectively. The polar plots show a high contrast in the SHG intensity, as for certain polarization angles the signal vanishes almost completely, which is an indication of the high quality of the samples.

A. Three-level model of $n = 1, 2$ states in a magnetic field

The magnetic field dependence of the three lowest exciton levels ($1S$, $2S$, and $2P$) can be analyzed by a three-level model. $2P$ excitons are excited by a dipole/dipole two-photon process. In a magnetic field in Voigt configuration, these even-parity excitons are coupled by the magneto-Stark effect to the odd-parity $1S$ and $2S$ excitons, and they can—due to this admixture—exhibit SHG by dipole emission. From the detailed SHG polarization dependences for MSE processes of the yellow and green series [29], one gets the SHG polarization dependences for the blue excitons. In Ref. [29], two-photon excited even-parity S excitons of the yellow series are coupled by the MSE to odd-parity P excitons, which lead to SHG by a dipole emission. Therefore, one expects the same SHG polarization dependences, since in both cases the SHG

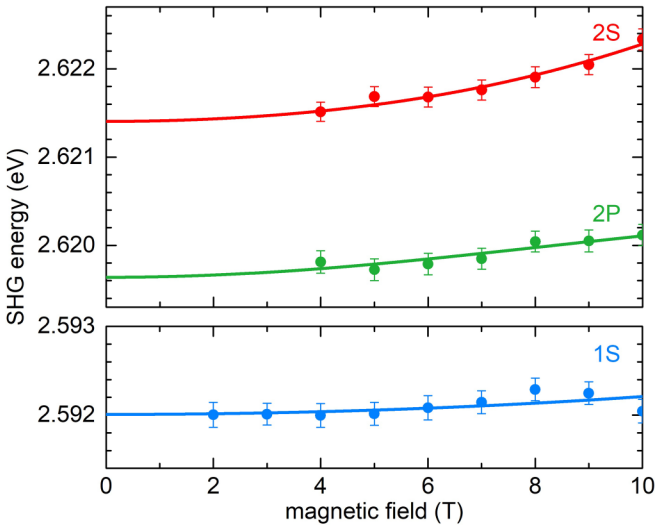

FIG. 9. Magnetic field dependence of exciton energies for an experimental geometry of $\mathbf{k} \parallel [1\bar{1}0]$ and $\mathbf{B} \parallel [110]$: Filled circles represent experimentally obtained energies by Gaussian fits to the second derivatives of the 1*S*, 2*P*, and 2*S* SHG spectra shown in Figs. 8(d), 8(e), and 8(f), respectively. The error bars take the spectral resolution and the Gaussian fit errors into account. The lines are fits according to the theory [Eq. (15)].

is due to a dipole/dipole excitation and a dipole emission process.

For an analysis of the magnetic field shift of this three-level system, one has to take into account two contributions: The diamagnetic shift ($\propto B^2$) and the repulsion between the states of opposite parity due to the MS-coupling ($\propto B$). The Hamiltonian for the 3-level system is given by the following 3×3 matrix:

$$\mathbf{M}_{\text{3-level}}(B) = \begin{pmatrix} E_{1S} + d_{1,0}B^2 & M_{1S2P}B & 0 \\ M_{1S2P}B & E_{2P} + d_{2,1}B^2 & M_{2S2P}B \\ 0 & M_{2S2P}B & E_{2S} + d_{2,0}B^2 \end{pmatrix}. \tag{15}$$

The matrix contains as diagonal entries the zero-field resonance energies E_{1S}, E_{2P}, and E_{2S} and the diamagnetic shift terms $d_{1,0}$, $d_{2,1}$, and $d_{2,0}$, which are given by [8]

$$\begin{aligned} H_{\text{dia}}(B) &= \frac{e^2}{8\mu_X}(x^2 + y^2)B^2 \\ &= \frac{e^2}{8\mu_X}\frac{2}{3}\langle r_{n,l}^2 \rangle B^2 \\ &= d_{n,l}B^2. \end{aligned} \tag{16}$$

Here only the shift coefficients for 1*S* ($n = 1, l = 0$), 2*S* ($n = 2, l = 0$), and 2*P* excitons ($n = 2, l = 1$) are relevant. The off-diagonal elements are given by the magneto-Stark interaction terms between the 1*S* and 2*P* and the 2*S* and 2*P*, which depend linearly on the magnetic field *B* and are given by M_{1S2P} and M_{2S2P} [29]. For $(x^2 + y^2)$ we introduce the average of the squared exciton radius $\langle r_{n,l}^2 \rangle = \frac{3}{2}(x^2 + y^2)$, which depends on the main quantum number *n* and the orbital quantum number *l* [52]:

$$\langle r_{n,l}^2 \rangle = \frac{a_0^2}{2} n^2 [5n^2 + 1 - 3l(l+1)]. \tag{17}$$

For the $d_{n,l}$ parameters in Eq. (15), we get

$$d_{n,l} = \frac{\langle r_{n,l}^2 \rangle}{\mu_X} \times 1.465\,68 \times 10^{-2}\ [\mu\text{eV T}^{-2}]. \tag{18}$$

With use of Eq. (17), we rewrite the $d_{n,l}$ parameters in terms of $\langle r_{1,0}^2 \rangle$ of the 1*S* exciton and get $d_{2,0} = 14 d_{1,0}$ and $d_{2,1} = 10 d_{1,0}$, which are inserted in Eq. (15). Our experimental results for the resonance energies are obtained by Gaussian fits to the second derivatives of the SHG spectra [Figs. 8(d), 8(e), and 8(f)] and are shown in Fig. 9 as filled circles. The fit according to the eigenvalues of Eq. (15) is shown as lines. From the fit we derive the zero-field energies of 1*S* and 2*S* exciton-polaritons and 2*P* exciton: $E_{1S} = 2.5920 \pm 0.0002$ eV, $E_{2S} = 2.6214 \pm 0.0002$ eV, and $E_{2P} = 2.6196 \pm 0.0002$ eV. As compared to the resonances measured by photoluminescence in Ref. [2], the 1*S* (2*S*) SHG resonance is shifted by 9.1 meV (0.5 meV) to higher energies, due to the polariton effect. We extract $d_{1,0} = 0.62 \pm 0.05\ \mu\text{eV T}^{-2}$, $M_{1S2P} = 0.106 \pm 0.004\ \mu\text{eV T}^{-1}$, and $M_{2S2P} = 0.43 \pm 0.02\ \mu\text{eV T}^{-1}$. Note that in contrast to the 2*P* state, the resonance energy of the 1*S* and 2*S* states is strongly influenced by the dipole-allowed exciton-photon interaction and shifted to the values on the upper polariton branches [see Fig. 5(b)].

It is expected that the coupling coefficients due to the MSE [Eq. (15)] are not influenced by the polariton effect, as the exciton content of the polariton states is not changed very much. The exciton content of the polariton states is almost 100%, as can be seen by the large damping [see Fig. 5(c)].

For the derivation of the reduced exciton mass from the data, we use the relation of reduced mass and exciton Bohr radius a_X from the simple hydrogen model

$$a_X = \varepsilon(E_{1S}) a_H / \mu_X, \tag{19}$$

where a_H is the hydrogen Bohr radius and $\varepsilon(E_{1S}) = 7.63$ is the dielectric constant at the energy of the 1*S* exciton from Eq. (A2). From Eqs. (17) and (18), the fit value for $d_{1,0} = 0.62(5)\ \mu\text{eV T}^{-2}$, and Eq. (19), we derive the reduced exciton mass $\mu_X = 0.226(6) m_0$, which agrees well with the value obtained in the polariton calculation of $\mu_X = 0.228 m_0$, and the exciton Bohr radius $a_X = 1.79(5)\ \mu\text{eV T}^{-2}$. In comparison, the yellow exciton has a reduced exciton mass of $\mu_{X,Y} = 0.363 m_0$ [53], and the Bohr radius of the yellow 1*S* exciton is $a_{X,Y} = 0.7$ nm [54].

TABLE II. Crossover magnetic field $B_{c,n}$ for *S* magnetoexcitons as a function of the principal quantum number *n* [Eq. (23)].

n	1	2	3	4	5	6	7	8
$B_{c,n}$ (T)	92	17	6.0	2.7	1.4	0.8	0.5	0.4

B. Magnetoexcitons in the high-field regime

In this section, we discuss experimental data on the energy shift of magnetoexciton states in high magnetic fields up to

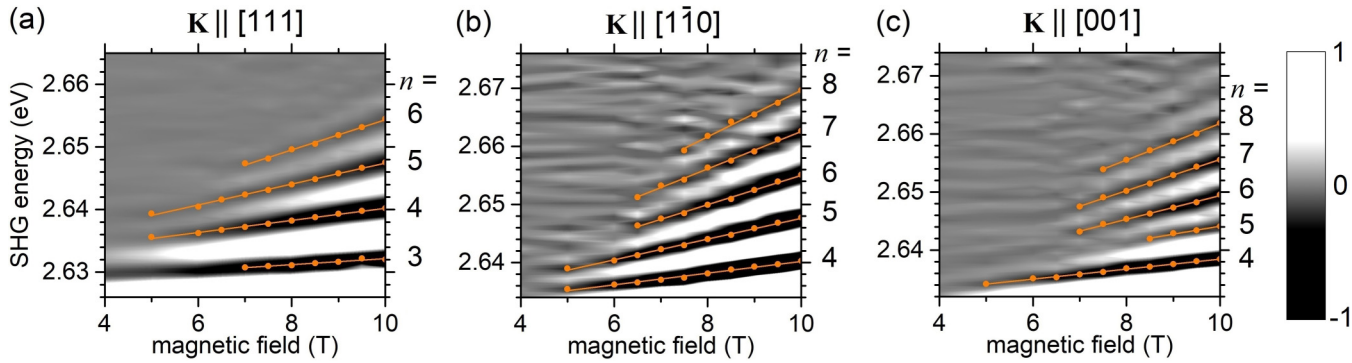

FIG. 10. Experimental results and fit of magnetic field dependence of magnetoexciton SHG spectra for different crystalline orientations: (a) **K** ∥ [111] and **B** ∥ [11$\bar{2}$], (b) **K** ∥ [1$\bar{1}$0] and **B** ∥ [110], (c) **K** ∥ [001] and **B** ∥ [110]; the rather broad resonances (see Fig. 7) are plotted as second derivatives. Circles mark the energies of the magnetoexcitons and lines show linear fits. By taking the second derivative of a SHG spectrum, a resonance peak with a negative curvature transforms into a minimum, which is represented by the black color. The sides of a resonance peak with positive curvature transform into maxima represented by the white color, as shown by the color scale.

10 T, the SHG spectra of which are shown in Fig. 7(a). The analysis of the shifts in the high-field regime allows us to evaluate the electron effective mass $m_{\mathbf{K}}^{8c}$ of the Γ_8^- conduction band for different crystal directions and the reduced exciton mass μ_X.

It is well established that in external magnetic fields, the optical spectra of semiconductors in the vicinity of the band gap are strongly contributed by diamagnetic excitons; for a review, see Refs. [55] and [56]. In the low-field regime, the exciton energies exhibit a B^2 dependence as given by the diamagnetic shift in Eq. (16). With increasing magnetic field the B^2 diamagnetic shift of exciton states is converted to a B-linear shift of magnetoexcitons in the high-field regime. In this regime, the cyclotron energies of electron and hole exceed their Coulomb interaction, and the energy shift ΔE of the magnetoexcitons is described similar to Landau levels by

$$\begin{aligned}\Delta E_n(B) &= \left(n-\tfrac{1}{2}\right)\hbar(\omega_{c,e}+\omega_{c,h}) \\ &= \left(n-\tfrac{1}{2}\right)\frac{\hbar e}{\mu_{\mathbf{K}}^{eh}}B, \end{aligned} \tag{20}$$

with the cyclotron frequencies $\omega_{c,e} = eB/m_{\mathbf{K}}^{8c}$ of the electron and $\omega_{c,h} = eB/m_{\mathbf{K}}^{7v}$ of the hole, the electron mass $m_{\mathbf{K}}^{8c}$ (Γ_8^- conduction band), the hole mass $m_{\mathbf{K}}^{7v}$ (Γ_7^+ valence band), and the reduced electron-hole mass are defined by

$$\frac{1}{\mu_{\mathbf{K}}^{\mathrm{eh}}} = \frac{1}{m_{\mathbf{K}}^{8c}} + \frac{1}{m^{7v}} \tag{21}$$

along the crystal direction **K**.

The low-field regime is converted to the high-field one at a crossover field $B_{c,n}$, at which the mean exciton radius

$$\langle r_{n,l}\rangle = \frac{a_0}{2}[3n^2 - l(l+1)] \tag{22}$$

and the magnetic length $l_n = \sqrt{\frac{2\hbar}{eB_{c,n}}(n-\frac{1}{2})}$ are equal to each other [44]. For S excitons, it is given by

$$B_{\mathrm{c},n} = \frac{8\hbar}{9ea_0^2}\frac{\left(n-\frac{1}{2}\right)}{n^4}, \tag{23}$$

with the exciton Bohr radius $a_X = \frac{\varepsilon}{\mu_X}a_H$, the hydrogen Bohr radius a_H, and the dielectric constant ε according to Eq. (A2). The values for $B_{c,n}$ calculated with the reduced mass $\mu_X = 0.226m_0$ obtained in Sec. IV A and the dielectric constants $\varepsilon(E_{Xi})$ given in Table I are listed in Table II. One can see that with the maximal magnetic field of 10 T used in our experiments, the high-field regime is valid for the exciton states with $n \geqslant 3$.

For a better visibility of the energy position of the magnetoexciton states, we plot the second derivatives of the SHG spectra versus magnetic field. These data are shown in Fig. 10 for a magnetic field range from 4 to 10 T in the energy region of the $n = 3$ to 8 blue exciton states. The results are shown for three different crystal orientations of **K** ∥ [111], **K** ∥ [1$\bar{1}$0], and **K** ∥ [001] in order to investigate the anisotropy effects. The energies of the magnetoexcitons are acquired by Gaussian fits to the second derivatives of the SHG spectra, and they are

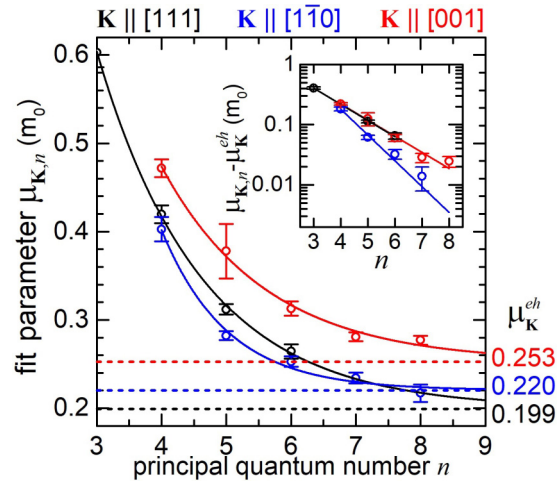

FIG. 11. Fit parameter $\mu_{\mathbf{K},n}$ as derived from slopes $s_{\mathbf{K},n}$ [Eq. (24)] as seen in Fig. 10. The error bars take the fit error of the slopes $s_{\mathbf{K},n}$ into account. The exponential fit of $\mu_{\mathbf{K},n}$ leads according Eq. (25) to reduced mass values $\mu_{\mathbf{K}}^{eh}$, as listed in Table III in the second column. The fit parameters are $a_{[001]} = 2.609$, $a_{[1\bar{1}0]} = 2.595$, and $a_{[111]} = 9.411$ in units of m_0 and $b_{[001]} = 0.617$, $b_{[1\bar{1}0]} = 0.620$, and $b_{[111]} = 0.987$. The inset shows a semilogarithmic plot of $\mu_{\mathbf{K},n} - \mu_{\mathbf{K}}^{eh}$ vs n for a better visualization of the exponential trend [59].

TABLE III. Experimentally derived values for the electron-hole reduced mass $\mu^{eh}_{\mathbf{K},\mathrm{exp}}$ and the effective electron mass $m^{8c}_{\mathbf{K},\mathrm{exp}}$ compared to the calculated values $m^{8c}_{\mathbf{K},\mathrm{theo},i}$ ($i = 1$ heavy and $i = 2$ light electron) of the split Γ_8^- conduction band from Ref. [11] for the three crystal directions $\mathbf{K} \parallel$ [111], [1$\bar{1}$0], and [001].

$\mathbf{K} \parallel$	$\mu^{eh}_{\mathbf{K}}(m_0)$	$m^{8c}_{\mathbf{K},\mathrm{exp}}(m_0)$	$m^{8c}_{\mathbf{K},\mathrm{theo},1}(m_0)$	$m^{8c}_{\mathbf{K},\mathrm{theo},2}(m_0)$
[111]	0.199(17)	0.304	0.261	0.241
[1$\bar{1}$0]	0.220(9)	0.356	0.332	0.201
[001]	0.253(14)	0.452	0.488	0.169

plotted as orange points. Their magnetic-field shift is fitted according to Eq. (20) and is shown by orange lines. From the slope

$$s_{\mathbf{K},n} = \frac{\hbar e\left(n - \frac{1}{2}\right)}{\mu_{\mathbf{K},n}} \tag{24}$$

of each magnetoexciton state we derive the fit parameter $\mu_{\mathbf{K},n}$. The $\mu_{\mathbf{K},n}$ are shown in Fig. 11 as open symbols and converge for increasing n to $\mu^{eh}_{\mathbf{K}}$ (dashed lines in Fig. 11).

The extrapolation can be done with a fit according to the empirical function

$$\mu_{\mathbf{K},n} = \mu^{eh}_{\mathbf{K}} + a_{\mathbf{K}} \exp\left(-b_{\mathbf{K}} n\right), \tag{25}$$

as shown by the solid lines in Fig. 11. In a semilogarithmic plot (inset) of $\mu_{\mathbf{K},n} - \mu^{eh}_{\mathbf{K}}$ versus n, one can see that the exponential function is a reasonable fit to the experimental data. The reduced masses obtained in that way are given in the second column in Table III. One can see that they show a considerable anisotropy changing from $0.199m_0$ for the [111] direction up to $0.253m_0$ for the [001] direction. From them we evaluate the conduction-band masses given in the third column using Eq. (21) and the value $m^{7v} = 0.575(50)m_0$ from Ref. [53], which also show remarkable anisotropy in the range from $0.304m_0$ up to $0.452m_0$.

TABLE IV. Our experimental results for parameters of blue excitons in Cu_2O compared to those of the experimental photoluminescence (PL) results of Ref. [2] and the theory results of Ref. [11]. $\mu_{X,1}$ is the reduced exciton mass obtained from the diamagnetic shift parameter in Sec. IV A, and $\mu_{X,2}$ is obtained from the magnetic shifts of the magnetoexcitons and the A parameters in Sec. IV B.

Parameter	This paper	[2] (PL)	[11] (theory)
E_{1S}	2.5920 eV		
E_{2S}	2.6214 eV		
E_{2P}	2.6196 eV		
E_{1S_T}	2.57926 eV	2.5829 eV	
E_{2S_T}	2.61921 eV	2.6209 eV	
E_g	2.6326 eV	2.6336 eV	
E_{Ryd}	57.1 meV	50.7 meV	
Γ_{1S}	13.9 meV	23.9 meV	
Γ_{2S}	7.64 meV	20.1 meV	
a_X	1.79 nm		
$\mu_{X,1}$	0.226 m_0		
$m^{8c}_{[111]}$	0.304 m_0		0.261 m_0
$m^{8c}_{[1\bar{1}0]}$	0.356 m_0		0.332 m_0
$m^{8c}_{[001]}$	0.452 m_0		0.488 m_0
$\mu_{X,2}$	0.195 m_0		

TABLE V. Parameters to calculate the background dielectric function from Ref. [46] at $T = 300$ K.

Parameter	Value	Parameter	Value
$E_{g,B}$	2.64 eV	Γ_B	0.05 eV
$E_{g,V}$	2.76 eV	Γ_V	0.05 eV
E_{1X}	3.45 eV	Γ_{1X}	0.36 eV
E_{1M}	4.25 eV	Γ_{1M}	0.36 eV
E_2	5.7 eV	Γ_2	0.32 eV
A_B	0.31 eV^2	B_{1X}	2.40 eV
A_V	0.516 eV^2	B_{1M}	1.75 eV
$E_{\mathrm{Ryd},B}$	0.05 eV	$\varepsilon_{1\infty}$	2.41
$E_{\mathrm{Ryd},V}$	0.05 eV	C_2	1.3
β_{1SV}	4.62×10^{-3}		

It is instructive to compare our results with band-structure calculations by spin density functional theory from Ref. [11]. As shown in Fig. 1, the Γ_8^- conduction band is divided into two subbands with different spatial dispersions, from which we obtain two sets of effective masses $m^{8c}_{\mathbf{K},\mathrm{theo},1}$ for the heavy and $m^{8c}_{\mathbf{K},\mathrm{theo},2}$ for the light electron. These masses are anisotropic and are listed for the different crystalline directions [111], [1$\bar{1}$0], and [001] in the fourth and fifth column in Table III. The experimental values for the conduction-band mass $m^{8c}_{\mathbf{K},\mathrm{exp}}$ are in good agreement with the theoretical results $m^{8c}_{\mathbf{K},\mathrm{theo},1}$ from Ref. [11] given in the fourth column of Table III. Therefore, the excited electrons occupy the states in the Γ_8^- subband with the larger effective mass.

With our results of the $m^{8c}_{\mathbf{K}}$, one can calculate the reduced exciton mass using the relations to the A parameters from Ref. [57], which are given by

$$m^{8c}_{[100]} = 1/(A_8 + A'_8), \tag{26}$$

$$m^{8c}_{[111]} = 1/(A_8 - A''_8), \tag{27}$$

$$m^{8c}_{[1\bar{1}0]} = 1/\left(A_8 - \tfrac{1}{2}\sqrt{A'^2_8 + 3A''^2_8}\right). \tag{28}$$

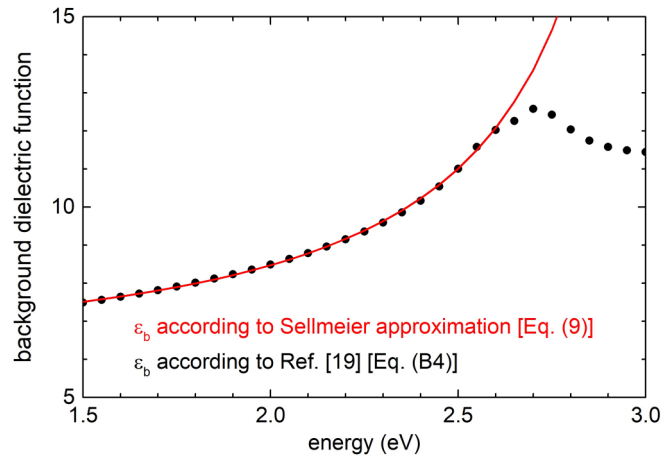

FIG. 12. Background dielectric function ε_b from Ref. [46] calculated according to Eq. (B4) (black dots) and the Sellmeier approximation Eq. (9) (red line) for a temperature of 300 K.

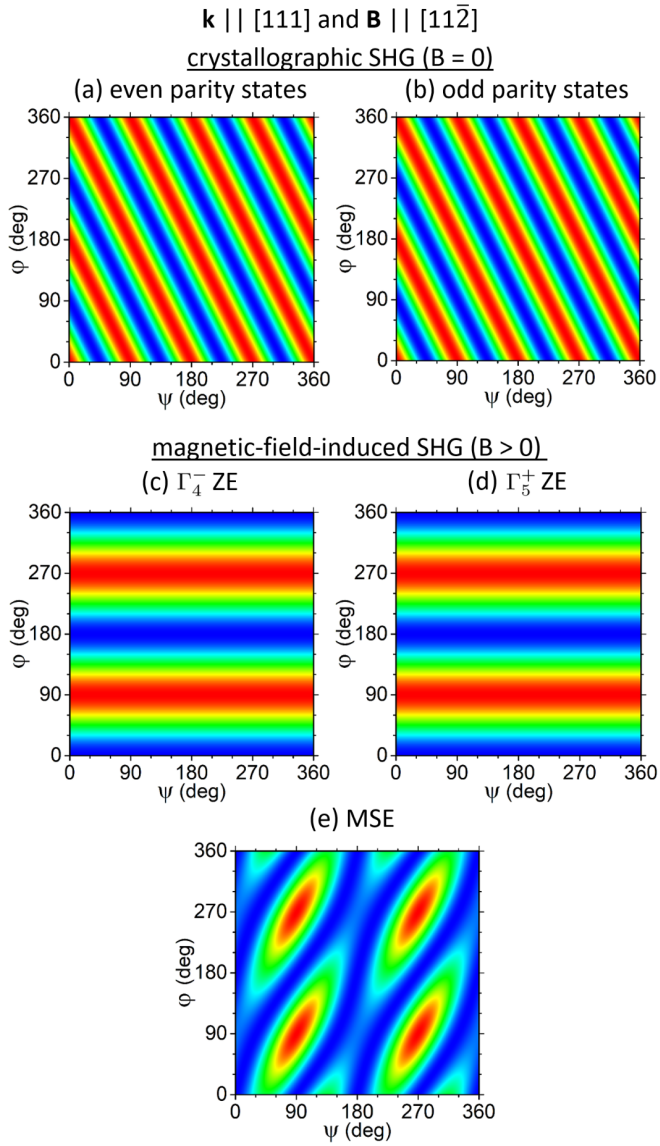

FIG. 13. 2D SHG polarization dependence for the relevant mechanisms as shown in Figs. 4 and 6 for the experimental configuration: **k** ∥ [111] and **B** ∥ [11$\bar{2}$].

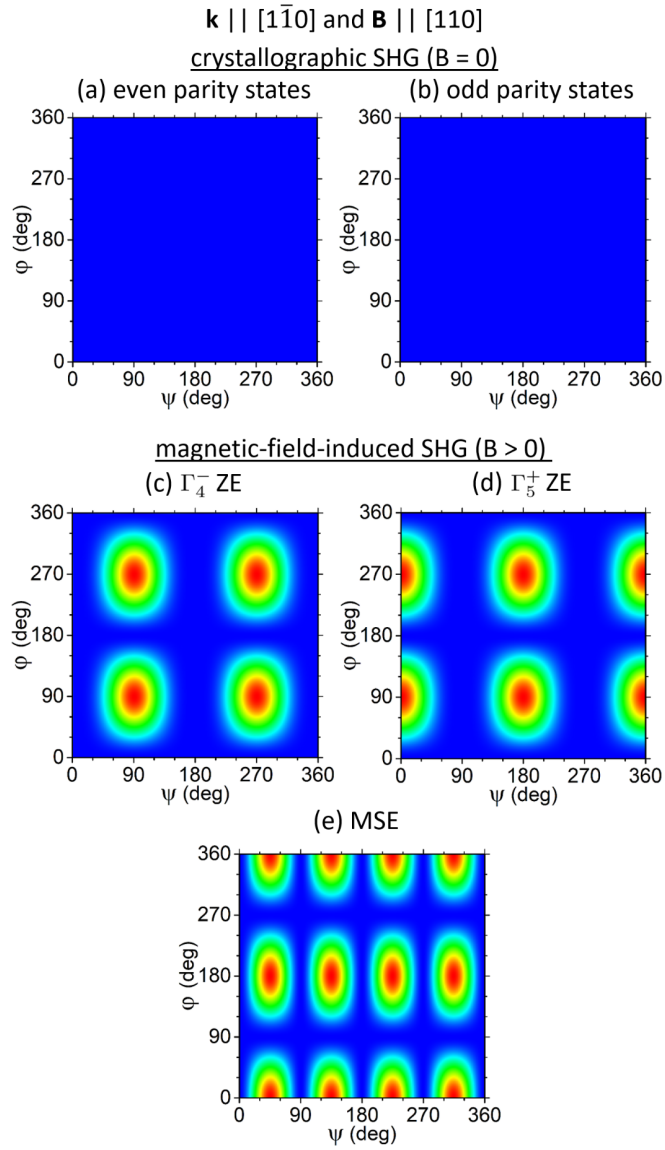

FIG. 14. 2D SHG polarization dependence for the relevant mechanisms as shown in Figs. 4 and 6 for the experimental configuration: **k** ∥ [1$\bar{1}$0] and **B** ∥ [110].

Solving this system of linear equations leads to $A_8 = 3.39(61)/m_0$, $A_8' = -1.17(75)/m_0$, and $A_8'' = 0.11(84)/m_0$, which agree quite well with those obtained from fitting the band structure [57]. The reduced exciton mass is then obtained from $1/\mu_X = 1/m^{7v} + A_8$ as $\mu_X = 0.195(24)m_0$.

The value of the reduced exciton mass from this analysis is in reasonable agreement with those derived from the polariton dispersion in Sec. III and the diamagnetic shift in Sec. IV A. The difference might reflect the effects of the nonparabolicity of the valence bands [58], which have not been included in the analysis.

V. CONCLUSIONS AND OUTLOOK

In this paper, we have presented nonlinear optical investigations of the blue exciton resonances in Cu_2O. The evaluated exciton parameters are listed in Table IV and compared to those of other publications. As compared to one-photon absorption experiments, which require evaporated layers of Cu_2O about 50 nm on, e.g., quartz substrates, which leads to strain effects [13], our SHG experiments allow measurements on oriented, strain-free mounted samples. The high quality of our samples is confirmed by a detailed polarization analysis. As shown in Sec. IV B, we are able to derive from magnetoexciton spectroscopy data on effective masses, which are compared to band-structure calculations. Because of their high oscillator strength density, the resonances have to be analyzed taking into account the polariton dispersion. As discussed in detail in Sec. III, the observed resonances fit the calculated polariton dispersion very well. Contrary to one-photon experiments, we are dealing with sharp momentum excitation ($\mathbf{k}_{\mathrm{SHG}} = 2\mathbf{k}_{\mathrm{laser}}$) and thus quasiparticle resonances in the two-photon SHG experiments. From the information of the analysis of the diamagnetic shift in the three-level model

of 1*S*, 2*S*, and 2*P* resonances (see Sec. IV A), we derive information on the ratio of the mean exciton radius squared to the reduced mass of the exciton, which was derived from the magnetoexciton analysis in Sec. IV B. From the analysis of our results from Secs. III and IV, we get a consistent set of parameters for the blue exciton resonances. The theoretical analysis of the magnetoexcitons can certainly be improved by a rigorous theoretical treatment, as was done for the yellow [60] and green series [61], where for the blue excitons the polariton dispersion would have to be taken into account.

As an outlook, we propose third-harmonic generation (THG) experiments to the odd parity blue and violet polariton resonances, since they are dipole-allowed, contrary to SHG, which are only quadrupole/dipole-allowed.

ACKNOWLEDGMENTS

We thank S. O. Krüger, Universität Rostock, for enlightening discussions. We acknowledge the financial support by the Deutsche Forschungsgemeinschaft through the International Collaborative Research Center TRR160 (Projects A8 and C8).

APPENDIX A: DETERMINATION OF THE EXCITON ENERGIES

The hydrogen model of excitons has to be corrected due to two effects: (i) nonparabolicity of the bands, and (ii) a frequency and wave-vector dependence of the dielectric function. A simple way to include the latter is to solve the implicit equation

$$E_{Bn} = \frac{1}{n^2}\frac{\mu_X}{\tilde{\varepsilon}(E_{Bn})^2}R_H, \tag{A1}$$

where $\tilde{\varepsilon}(E)$ is the energy-dependent dielectric function, μ_X is the reduced exciton mass, and $R_H = 13.605\,693$ eV is the Rydberg constant.

The dielectric function in the region between 0 and 100 meV is determined by LO phonons and given as [49]

$$\frac{\tilde{\varepsilon}(E)}{\tilde{\varepsilon}_b} = \prod_i \frac{\left(\hbar^2\omega_{L,i}^2 - E^2\right)}{\left(\hbar^2\omega_{T,i}^2 - E^2\right)}, \tag{A2}$$

where $\tilde{\varepsilon}_b = 6.53$ is the dielectric constant above the infrared region, and $\hbar\omega_{L,i}$ and $\hbar\omega_{T,i}$ ($i = 1, 2$) are the LO and TO phonon energies: $E_{\mathrm{TO1}} = 18.8$ meV, $E_{\mathrm{LO1}} = 19.1$ meV, $E_{\mathrm{TO2}} = 78.5$ meV, and $E_{\mathrm{LO2}} = 82.1$ meV. To obtain agreement with the measured 1*S* (2.5920 eV) and 2*S* (2.6214 eV) energies for the blue excitons, we have to use $\mu_X = 0.228m_0$. This results in a binding energy of 53.30 me V for the 1*S* exciton [$\tilde{\varepsilon}(1S) = 7.63$] and 13.35 me V for the 2*S* state [$\tilde{\varepsilon}(2S) = 7.62$] as given in the main text. Note that the exciton Rydberg energy, which is defined as the limiting value of Eq. (A1) for $n \to \infty$, is $E_{\mathrm{Ryd}} = 57.1$ meV (dielectric constant of 7.37).

APPENDIX B: BACKGROUND DIELECTRIC CONSTANT

Due to the large oscillator strength density of the violet exciton transitions and dominant contributions from exciton states at the *X* and *M* point (Sec. III of Ref. [46]) above the blue exciton states, the background dielectric constant ε_b is varying across the spectral range of the blue exciton states. In Ref. [46], a thorough analysis of the dielectric function in Cu_2O at room temperature is presented. We neglect the temperature dependence of the dielectric function, as our experiments are performed at $T = 1.4$ K. This allows us to derive the correct expression for the dielectric function.

We take the following transitions (the parameters are given in Table V) into account:

(i) Blue and violet transitions with gap energies $E_{g,B}$ and $E_{g,V}$ at which the transition into the corresponding continuum starts. The contribution of the continuum to the dielectric constant is given by [46]

$$\varepsilon_{BV}(E) = \sum_{\alpha=B,V} \frac{A_\alpha E_{0\alpha}}{4E_{\mathrm{Ryd},0\alpha}(E + i\Gamma_\alpha)} \ln \frac{E_{0\alpha}^2}{E_{0\alpha}^2 - (E + i\Gamma_\alpha)^2}, \tag{B1}$$

with the exciton ground-state energies $E_{0,B} = E_{g,B} - E_{\mathrm{Ryd},B}$ and $E_{0,V} = E_{g,V} - E_{\mathrm{Ryd},V}$, the exciton Rydberg energies $E_{\mathrm{Ryd},\alpha}$, the oscillator strength density related parameters A_α, and damping constants Γ_α. The transitions into the blue exciton states themselves have to be omitted, as these are contained in the polaritons. The contribution of the 1*S* violet state is similar to Eq. (8).

(ii) The transitions at the *X* and *M* points can be described as two-dimensional excitons, where only the ground states are taken into account. Their contribution to the dielectric constant can be written as

$$\varepsilon_{XM}(E) = -\sum_{\alpha=X,M} \frac{B_{1\alpha}}{E_{1\alpha} - E - i\Gamma_{1\alpha}}. \tag{B2}$$

(iii) The last transition to be considered is of E_2 type and of the form

$$\varepsilon_{E_2}(E) = \frac{C_2E_2^2}{(E_2 - E)^2 - i\Gamma_2E_2E}. \tag{B3}$$

(iv) All other higher-lying transitions can be approximated by a constant contribution $\varepsilon_{1\infty}$ to the dielectric function.

The background dielectric function is then given by

$$\varepsilon_b(E) = \varepsilon_{B,V}(E) + \varepsilon_{XM}(E) + \varepsilon_{E_2}(E) + \varepsilon_{1\infty}. \tag{B4}$$

Due to the forbidden character of the yellow and green excitons [14], the absorption is quite small below the blue exciton states, and we neglect the imaginary part of the dielectric function. The values for all parameters are given in Table V. Figure 12 shows the background dielectric function calculated from the above expressions (red line) and the Sellmeier approximation Eq. (9) (black dots).

APPENDIX C: 2D POLARIZATION DIAGRAMS OF SHG MECHANISMS

For two experimental configurations $\mathbf{k} \parallel [111]$, $\mathbf{B} \parallel [11\bar{2}]$ and $\mathbf{k} \parallel [1\bar{1}0]$, $\mathbf{B} \parallel [110]$, which are discussed in Sec. IV, the 2D SHG polarization diagrams are shown in Figs. 13 and 14 for each mechanism addressed in Figs. 4 and 6.

[1] E. F. Gross, Excitons and their motion in crystal lattices, Sov. Phys. Usp. **5**, 2 (1962).

[2] M. Takahata and N. Naka, Photoluminescence properties of the entire excitonic series in Cu_2O, Phys. Rev. B **98**, 195205 (2018).

[3] M. A. M. Versteegh, St. Steinhauer, J. Bajo, T. Lettner, A. Soro, A. Romanova, S. Gyger, L. Schweickert, A. Mysyrowicz, and V. Zwiller, Giant Rydberg excitons in Cu_2O probed by photoluminescence excitation spectroscopy, arXiv:2105.07942.

[4] M. Aßmann and M. Bayer, Semiconductor Rydberg physics, Adv. Quantum Technol. **3**, 1900134 (2020).

[5] T. Kazimierczuk, D. Fröhlich, S. Scheel, H. Stolz, and M. Bayer, Giant Rydberg excitons in the copper oxide Cu_2O, Nature (London) **514**, 343 (2014).

[6] R. J. Elliott, Symmetry of excitons in Cu_2O, Phys. Rev. **124**, 340 (1961).

[7] J. Brandt, D. Fröhlich, Ch. Sandfort, M. Bayer, H. Stolz, and N. Naka, Ultranarrow Optical Absorption and Two-Phonon Excitation Spectroscopy of Cu_2O Paraexcitons in a High Magnetic Field, Phys. Rev. Lett. **99**, 217403 (2007).

[8] R. S. Knox, *Introduction to Exciton Physics* (Academic, New York, 1963).

[9] J. P. Dahl and A. C. Switendick, Energy bands in cuprous oxide, J. Phys. Chem. Solids **27**, 931 (1965).

[10] J. Robertson, Electronic structure and x-ray near-edge core spectra of Cu_2O, Phys. Rev. B **28**, 3378 (1983).

[11] M. French, R. Schwarz, H. Stolz, and R. Redmer, Electronic band structure of Cu_2O by spin density functional theory, J. Phys.: Condens. Matter **21**, 015502 (2009).

[12] L. Y. Isseroff and E. A. Carter, Importance of reference Hamiltonians containing exact exchange for accurate one-shot *GW* calculations of Cu_2O, Phys. Rev. B **85**, 235142 (2012).

[13] A. Daunois, J. L. Deiss, and B. Meyer, Étude spectrophotométrique de l'absorption bleue et violette de Cu_2O, J. Phys. France **27**, 142 (1966). Note that in the paper both blue and violet excitons are split by strain into a doublet. Therefore, one has to add the oscillator strength of both components to get the values given.

[14] I. Pastrnyak, Absorption, reflection, and nature of the electron optical transitions in Cu_2O crystals, Sov. Phys. Solid State **3**, 633 (1961).

[15] Y. Sun, K. Rivkin, J. Chen, J. B. Ketterson, P. Markworth and R. P. Chang, Strain splitting of 1*s* yellow orthoexciton of epitaxial orthorhombic Cu_2O films on MgO [110], Phys. Rev. B **66**, 245315 (2002).

[16] B. Borie, C. J. Sparks, and J. V. Cathcart, Epitaxially induced strains in Cu_2O films on copper single crystals - I X-ray diffraction effects, Acta Metall. **10**, 691 (1962).

[17] D. Fröhlich, J. Brandt, C. Sandfort, M. Bayer, and H. Stolz, High resolution spectroscopy of excitons in Cu_2O, Phys. Status Solidi B **243**, 2367 (2006).

[18] L. C. Andreani, in *Confined Electrons and Photons: New Physics and Applications*, edited by C. Weisbuch and E. Burstein (Plenum, New York, 1995), p. 57.

[19] J. Schmutzler, D. Fröhlich, and M. Bayer, Signatures of coherent propagation of blue polaritons in Cu_2O, Phys. Rev. B **87**, 245202 (2013).

[20] M. Y. Shen, *The Principles of Nonlinear Optics* (Wiley, New York, 2003).

[21] R. W. Boyd, *Nonlinear Optics* (Academic/Elsevier, Burlington, 2008).

[22] E. Hanamura, Y. Kawabe, and A. Yamanaka, *Quantum Nonlinear Optics* (Springer, Berlin, 2007).

[23] D. R. Yakovlev, V. V. Pavlov, A. V. Rodina, R. V. Pisarev, J. Mund, W. Warkentin, and M. Bayer, Exciton spectroscopy of semiconductors by the method of optical harmonics generation (Review), Phys. Solid State **60**, 1471 (2018).

[24] I. Sänger, D. R. Yakovlev, B. Kaminski, R. V. Pisarev, V. V. Pavlov, and M. Bayer, Orbital quantization of electronic states in a magnetic field as the origin of second-harmonic generation in diamagnetic semiconductors, Phys. Rev. B **74**, 165208 (2006).

[25] M. Lafrentz, D. Brunne, A. V. Rodina, V. V. Pavlov, R. V. Pisarev, D. R. Yakovlev, A. Bakin, and M. Bayer, Second harmonic generation spectroscopy of excitons in ZnO, Phys. Rev. B **88**, 235207 (2013).

[26] W. Warkentin, J. Mund, D. R. Yakovlev, V. V. Pavlov, R. V. Pisarev, A. V. Rodina, M. A. Semina, M. M. Glazov, E. L. Ivchenko, and M. Bayer, Third harmonic generation on exciton-polaritons in bulk semiconductors subject to a magnetic field, Phys. Rev. B **98**, 075204 (2018).

[27] J. Mund, D. R. Yakovlev, M. A. Semina, and M. Bayer, Optical harmonic generation on the exciton-polariton in ZnSe, Phys. Rev. B **102**, 045203 (2020).

[28] J. Mund, D. Fröhlich, D. R. Yakovlev, and M. Bayer, High-resolution second harmonic generation spectroscopy with femtosecond laser pulses on excitons in Cu_2O, Phys. Rev. B **98**, 085203 (2018).

[29] A. Farenbruch, J. Mund, D. Fröhlich, D. R. Yakovlev, M. Bayer, M. A. Semina, and M. M. Glazov, Magneto-Stark and Zeeman effect as origin of second harmonic generation of excitons in Cu_2O, Phys. Rev. B **101**, 115201 (2020).

[30] A. Farenbruch, D. Fröhlich, D. R. Yakovlev, and M. Bayer, Two-photon absorption and second harmonic generation of 1*S* para- and orthoexcitons in Cu_2O coupled by a magnetic field, Phys. Rev. B **102**, 115203 (2020).

[31] A. Farenbruch, D. Fröhlich, D. R. Yakovlev, and M. Bayer, Rydberg Series of Dark Exciton in Cu_2O, Phys. Rev. Lett. **125**, 207402 (2020).

[32] N. Naka and N. Nagasawa, High precision two-photon spectroscopy on emission of 1*s* ortho-excitons in Cu_2O, Solid State Commun. **110**, 153 (1999).

[33] N. Naka and N. Nagasawa, Experimental study on two-photon oscillator strength of hydrogenic yellow excitons in Cu_2O, Solid State Commun. **116**, 417 (2000).

[34] S. Kono, N. Naka, M. Hasuo, S. Saito, T. Suemoto, and N. Nagasawa, Coherent optical processes of 1*s* ortho-excitons in Cu_2O by two-photon excitations, Solid State Commun. **97**, 455 (1996).

[35] D. Fröhlich, K. Reimann, and R. Wille, Time-resolved two-photon emission in Cu_2O, Europhys. Lett. **3**, 853 (1987).

[36] T. Goto, M. Y. Shen, S. Koyama, and T. Yokouchi, Bose-Einstein statistics of orthoexcitons generated by two-photon resonant absorption in cuprous oxide, Phys. Rev. B **56**, 4284(E) (1997).

[37] Y. Liu and D. Snoke, Resonant two-photon excitation of 1*s* paraexcitons in cuprous oxide, Solid State Commun. **134**, 159 (2005).

[38] D. Fröhlich, Two- and three-photon spectroscopy of solids, in *Nonlinear Spectroscopy of Solids: Advances and Applications*, edited by B. Di Bartolo and B. Bowlby (Plenum, New York, 1994), p. 289.

[39] L. Frazer, R. D. Schaller, K. B. Chang, J. B. Ketterson, and K. R. Poeppelmeier, Third-harmonic generation in cuprous oxide: efficiency determination, Opt. Lett. **39**, 618 (2014).

[40] J. Heckötter, J. Thewes, D. Fröhlich, M. Aßmann, and M. Bayer, Landau-level quantization of the yellow excitons in cuprous oxide, Phys. Solid State **60**, 1625 (2018).

[41] D. Ziemkiewicz, G. Czajkowski, K. Karpiński, and S. Zielińska-Raczyńska, Rydberg magnetoexcitons in Cu_2O quantum wells, Phys. Rev. B **103**, 035305 (2021).

[42] S. Zielińska-Raczyńska, D. A. Fishman, C. Faugeras, M. M. P. Potemski, P. H. M. van Loosdrecht, K. Karpiński, G. Czajkowski, and D. Ziemkiewicz, Magneto-excitons in Cu_2O: theoretical model from weak to high magnetic fields, New J. Phys. **21**, 103012 (2019).

[43] A. E. Siegmann, *Lasers* (University Science Books, Mill Valley, 1986).

[44] J. Heckötter, M. Freitag, D. Fröhlich, M. Aßmann, M. Bayer, M. A. Semina, and M. M. Glazov, Scaling laws of Rydberg excitons, Phys. Rev. B **96**, 125142 (2017).

[45] J. Heckötter, M. Freitag, D. Fröhlich, M. Aßmann, M. Bayer, M. A. Semina, and M. M. Glazov, High-resolution study of the yellow excitons in Cu_2O subject to an electric field, Phys. Rev. B **95**, 035210 (2017).

[46] T. Ito, T. Kawashima, H. Yamaguchi, T. Masumi, and S. Adachi, Optical properties of Cu_2O studied by spectroscopic ellipsometry, J. Phys. Soc. Jpn. **67**, 2125 (1998).

[47] D. Boggett and R. Loudon, Theory of Two-Photon Absorption by Polaritons, Phys. Rev. Lett. **28**, 1051 (1972).

[48] D. Boggett and R. Loudon, Theory of exciton-polariton generation by two-photon absorption, J. Phys. C **6**, 1763 (1973).

[49] H. Stolz, F. Schöne, and D. Semkat, Interaction of Rydberg excitons in cuprous oxide with phonons and photons: Optical linewidth and polariton effect, New J. Phys. **20**, 023019 (2018).

[50] K. Cho, Reflectance spectrum of multi-component polaritons, Solid State Commun. **27**, 305 (1978).

[51] W. C. Tait, Quantum theory of a basic light-matter interaction, Phys. Rev. B **5**, 648 (1972).

[52] T. F. Gallagher, *Rydberg Atoms* (Cambridge University Press, Cambridge, 1994).

[53] N. Naka, I. Akimoto, M. Shirai, and K. Kan'no, Time-resolved cyclotron resonance in cuprous oxide, Phys. Rev. B **85**, 035209 (2012).

[54] G. M. Kavoulakis, Y.-C. Chang, and G. Baym, Fine structure of excitons in Cu_2O, Phys. Rev. B **55**, 7593 (1997).

[55] R. P. Seisyan and B. P. Zakharchenja, in *Landau Level Spectroscopy*, edited by G. Landwehr and E. I. Rashba, Interband Magneto-optics of Semiconductors as Diamagnetic Exciton Spectroscopy (Elsevier, Amsterdam, 1991), Chap. 7, p. 354.

[56] R. P. Seisyan, Diamagnetic excitons and exciton magnetopolaritons in semiconductors, Semicond. Sci. Technol. **27**, 053001 (2012).

[57] S. O. Krüger and S. Scheel, Interseries transitions between Rydberg excitons in Cu_2O, Phys. Rev. B **100**, 085201 (2019).

[58] F. Schöne, S. O. Krüger, P. Grünwald, H. Stolz, S. Scheel, M. Aßmann, J. Heckötter, J. Thewes, D. Fröhlich, and M. Bayer, Deviations of the exciton level spectrum in Cu_2O from the hydrogen series, Phys. Rev. B **93**, 075203 (2016).

[59] $\mu_{[1\bar{1}0],8}$ is negative and can therefore not be shown in a logarithmic plot.

[60] F. Schweiner, J. Main, G. Wunner, and Ch. Uihlein, Even exciton series in Cu_2O, Phys. Rev. B **95**, 195201 (2017).

[61] P. Rommel, P. Zielinski, and J. Main, Green exciton series in cuprous oxide, Phys. Rev. B **101**, 075208 (2020).